

# **Temperature and pressure variability in mid-latitude low atmosphere and stratosphere-ionosphere coupling**

**A. L. Morozova<sup>1</sup>, P. Ribeiro<sup>1,2</sup>, J. J. Blanco<sup>3</sup>, and T.V. Barlyaeva<sup>1</sup>**

<sup>1</sup>CITEUC, University of Coimbra, Almas de Freire, Sta. Clara, Coimbra, 3040-004, Portugal.

<sup>2</sup> Geophysical and Astronomical Observatory, University of Coimbra, Almas de Freire, Sta. Clara, Coimbra, 3040-004, Portugal.

<sup>3</sup> University of Alcalá, Pza. San Diego, s/n, 28801 Alcalá de Henares, Madrid, Spain.

Corresponding author: Anna Morozova (annamorozovauc@gmail.com)

## **Key Points:**

- Temperature and pressure at 70-10 hPa levels found to anti-correlate with the ionospheric total electron content
- The stratosphere-ionosphere coupling is stronger in winter, especially during an east-QBO phase with a sudden stratospheric warming event
- The stratospheric-ionospheric coupling is tested with different mathematical approaches including the convergent cross mapping analysis

## Abstract

This study presents the continuation of the analysis of variations of atmospheric and space weather parameters above Iberian Peninsula along two years near the 24<sup>th</sup> solar cycle maximum presented in *Morozova et al.* [2016]. Previously, the first mode of the principal component analysis was shown to correlate with the lower stratospheric ozone and anti-correlate with cosmic ray flux. In this paper we discuss the second mode that, to our mind, suggests a coupling between the stratosphere and ionosphere.

This second mode, located in the low and middle stratosphere and explaining ~6-15% of temperature and ~2.5% of geopotential height variations, positively correlates with the middle-stratospheric ozone content. Among locally measured space weather parameters, this atmospheric mode negatively correlates with the ionospheric total electron content.

The stratospheric-ionospheric coupling was analyzed using the correlation and wavelet analyses. The found similarities between variations of the stratospheric and ionospheric parameters were tested with a method allowing estimation of the causal nature of the found relationships – the convergent cross mapping (CCM). Strong evidences for the stratospheric-ionospheric coupling were obtained for the winter 2012-2013 that is characterized by the east QBO phase and a strong sudden stratospheric warming event.

## 1 Introduction

The ionosphere is a partially ionized layer of the Earth's atmosphere located between the upper mesosphere (~ 60 km) and the lower exosphere (~ 900 km). In this paper we focus on the variations of the ionospheric parameters at middle latitudes. Here, the main ionization sources in the upper atmosphere are the solar UV and XR radiations, and energetic particles of the solar and cosmic origin. The ionosphere shows coupling both with the underlying neutral atmosphere and the overlying magnetosphere [*Chapman and Bartels*, 1951; *Kazimirovsky and Kokourov*, 1991]. Electric currents running in the ionosphere cause variations of the ground measured geomagnetic field, e.g., well known “solar quiet” (Sq) daily variations [*Chapman and Bartels*, 1951; *Matsushita*, 1968; *Yamazaki et al.*, 2016]. On the other hand, geomagnetic storms cause both increase and decrease of the peak electron density of the ionospheric F2 layer [*Martyn*, 1953; *Sato*, 1957; *Cander*, 2016]. Understanding of variations of ionospheric parameters is not only scientifically important but also necessary from the practical and technological points of view. Variations in ionospheric plasma densities change conditions for the radio signal propagations and, consequently, affect the functioning of the satellite based communication, surveillance, and navigation systems [e.g., *Kumar and Parkinson*, 2017].

The most widely used parameters characterizing ionospheric variable conditions are the total electron content (TEC, i.e. total number of electrons in a column of air of 1 m<sup>2</sup> cross section) and the critical frequency of the ionospheric layer F2 ( $f_0F2$ , i.e. a direct measure of the peak electron density  $N_mF2$  provided by vertical incidence ionosondes). The ionospheric parameters have been shown to be influenced by many factors, both external, such as the solar irradiance and energy input from the magnetosphere, and internal, e.g., changes in the phase and amplitude of the atmospheric waves and tides [*Forbes et al.*, 2000; *Pedatella and Forbes*, 2010].

First of all, the ionization level varies with the solar UV flux showing both regular variations on hourly (changes of the insolation during the day), seasonal (Earth's rotation around the Sun) and decadal (e.g. due to solar cycles) time scales, and sporadic changes due to, e.g., solar UV flares [e.g. *Rishbeth et al.*, 2000; *Maruyama et al.*, 2009; *Roux et al.*, 2012].

The ionospheric parameters are also strongly affected by magnetospheric conditions, especially during geomagnetic storms (defined as a decrease greater than 100 nT of the horizontal component of the geomagnetic field measured at the surface of the Earth, e.g., *Cander and Mihajlovic* [1998]). In a very recent paper, *Kumar and Parkinson* [2017] studied the  $N_mF2$  ( $f_0F2$ ) perturbations with respect to the local time at geomagnetic storm onset, season, and the storm intensity. They found that the storm-associated depletions (negative storm effects) and enhancements (positive storm effects) are driven by different but related physical mechanisms, although the depletion mechanism tends to dominate over the enhancement one. The negative storm effects were found to start immediately after geomagnetic storm onset in the nightside high-latitude ionosphere, while the depletions in the dayside high-latitude ionosphere are delayed by a few hours. The equatorward expansion of negative storm effects is found to be regulated by storm intensity (farthest equatorward and deepest during intense storms), season (largest in summer), and time of a day (generally deeper on the nightside). In contrast, positive storm effects typically occur on the dayside mid-latitude and low-latitude ionospheric regions when the storms are in the main phase, regardless of the season. Since, at middle latitudes, TEC usually increases during the initial and main phases of a geomagnetic storm and decreases during the recovery phase [*Roux et al.*, 2012; *Cander*, 2016], it is expected for TEC to anti-correlate with the geomagnetic Dst index and ground measured horizontal component of geomagnetic field [*Roux et al.*, 2012].

On the other hand, the neutral component (coupled with the ionized one [*Kazimirovsky et al.*, 2003; *Leake*, 2014]) of the upper atmosphere and ionosphere is affected by conditions in the lower atmosphere (stratosphere and even upper troposphere) as different waves and tides propagate upward into the upper atmosphere. These waves and tides travel both between different latitudes and between atmospheric layers [*Rishbeth et al.*, 2000; *Maruyama et al.*, 2009; *Yamazaki et al.*, 2016]. These atmospheric forcings were shown [*Kazimirovsky et al.*, 2003; *Laštovička et al.*, 2012] to be responsible for variations of ionospheric parameters, e.g.,  $f_0F2$  and TEC. *Forbes et al.* [2000] argued that ~15-20% of the observed ionospheric variability at all latitudes with periods in a range of ~2-30 days under quiet geomagnetic conditions appears to have meteorological origin. The stratosphere–ionosphere coupling was not only observed at different latitudes and during different time intervals, but simulated using modern atmospheric and atmosphere-ionosphere models [e.g., *Mendillo et al.*, 2002; *Pedatella*, 2016; *Gavrilov et al.*, 2018; *Pedatella and Liu*, 2018].

The hypothesis that the ionosphere can be forced by conditions in the lowest parts of the Earth's atmosphere (stratosphere and upper troposphere) was thoroughly tested during the last decade [e.g., *Laštovička*, 2006; *Laštovička et al.*, 2006; *Liu et al.*, 2010; *Yiğit et al.*, 2016; see also a review about the ionosphere-stratosphere coupling and the role in it of atmospheric tides and waves by *Kazimirovsky et al.*, 2003 and references therein]. Planetary and gravity waves, and atmospheric tides were pointed out as the most probable forcing agents [*Fritts and Alexander*, 2003; *Laštovička*, 2003 and 2006; *Ern et al.*, 2016]. The amplitudes and periods of such waves/tides change when they propagate toward the upper and less dense atmosphere and interact with the upper atmospheric tides and acoustic waves [*Fritts and Alexander*, 2003; *Laštovička*, 2006; *Ern et al.*, 2016; *Snively*, 2017]. This kind of coupling is seen not only in polar regions but also in the middle and even equatorial latitudes [*Altadill and Apostolov*, 2001 and 2003; *Pancheva and Mitchell*, 2004; *Liu et al.*, 2010; *Ern et al.*, 2016; see also review by *Yiğit et al.*, 2016 and references therein]. Since conditions in the winter stratosphere at middle to high latitudes favor the upward propagation of the atmospheric waves [*Fritts and Alexander*, 2003], the ionospheric response to the stratospheric forcing is more prominent during the cold months.

One of the interesting phenomena related to the ionosphere-stratosphere coupling through atmospheric waves and tides is the observation of variations of ionospheric parameters during specific events in the polar stratosphere (most often seen in the Northern Hemisphere) named sudden stratospheric warmings (SSW). SSW is defined as a sudden and fast warming of the polar stratosphere accompanied by changes of the strength and direction of the stratospheric zonal wind at 60°N [Coy and Pawson, 2015]. The ionospheric response to SSW is frequently seen at the middle, low and equatorial latitudes in variations of TEC,  $f_0F_2$  and other ionospheric parameters [Goncharenko *et al.*, 2013; Jonah *et al.*, 2014; Knížová *et al.*, 2015; Shpynev *et al.*, 2015; Chen *et al.*, 2016].

The stratosphere–ionosphere coupling is usually associated with changes of the phase and amplitude of the atmospheric tides (especially, semidiurnal tides as is shown, e.g., in Pedatella and Forbes, 2010) and also waves with periods of 2–23 days that are strongly amplified in winter atmosphere and during SSW in the vicinity of jet streams, frontal systems and mountain ridges [Altadill and Apostolov, 2001 and 2003; Fritts and Alexander, 2003; Pancheva and Mitchell, 2004; Goncharenko *et al.*, 2013; Knížová *et al.*, 2015; Bramberger *et al.*, 2017]. The ionospheric response is more prominent during the strong SSW events [Pancheva and Mukhtarov, 2011]. Sometimes this effect is seen in the ionospheric parameters a couple days before the maximum of a SSW event [as is shown for the SSW event in 2008 by Goncharenko and Zhang, 2008], reflecting perturbations that take place in the polar stratosphere and mesosphere during the pre-SSW and SSW periods. Moreover, the response of the ionosphere to a geomagnetic disturbance can be significantly affected by the lower atmosphere during periods of SSW [Pedatella, 2016; Pedatella and Liu, 2018].

Another phenomenon of the lower atmosphere that can affect ionosphere–stratosphere coupling is the quasi-biennial oscillations (QBO) of the direction of the stratospheric zonal winds near the equator. The QBO phase (west or east,  $wQBO$  or  $eQBO$ , respectively) affect the propagation conditions for gravity waves in the lower and middle atmosphere [Lu *et al.*, 2008] and, therefore, the polar vortex conditions (e.g., so-called Holton and Tan effect, Holton and Tan [1982]). SSWs are more frequent during the  $eQBO$  epoch, whereas  $wQBO$  periods are associated with stronger and longer living polar vortex, and strong westward zonal winds in the mid-latitudinal stratosphere [Lu *et al.*, 2008]. Thus, we can expect dependence of the ionosphere–stratosphere coupling strength on the QBO phase due to, for instance, changes in the amplitude of some atmospheric tides [Yamazaki *et al.*, 2016].

In this paper, we present the continuation of our previous analysis [Morozova *et al.*, 2017] of couplings between the locally measured atmospheric and space weather parameters. In the previous paper we analyzed the first mode of variations of tropospheric and lower stratospheric temperature and pressure fields over a mid-latitudinal region (Iberian Peninsula). This mode was shown to be related, in particular, to variations of the lower stratospheric ozone content ( $O_3$  at 50 hPa level, hereafter  $O_3_{50}$ ) and the locally measured cosmic ray (CR) flux. In this paper we will focus on the second mode that shows covariability with middle stratospheric ozone content ( $O_3$  at 10 hPa level) and geomagnetic and ionospheric parameters, but weak or none covariability with the CR flux or lower stratospheric ozone ( $O_3_{50}$ ). Since this mode, as is shown below in sec. 5, is more prominent during cold season (approximately, from November to April), we are going to focus on the relations between the atmospheric and geophysical parameters during two winters: 2012–2013 and 2013–2014 (hereafter,  $eQBO/SSW$  winter and  $wQBO$  winter, respectively). The first one is characterized by the east QBO phase and a strong SSW event in the beginning of January 2013 [January 6–7, Butler *et al.*, 2017]. During the second winter no significant SSW was observed and the QBO was in the west phase. Unfortunately, the chosen time interval does not allow to separate the effect from the SSW event and the east QBO phase.

The paper is organized as follows: section 2 contains the descriptions of the analyzed data sets, and section 3 describes the applied mathematical methods. General description of the space weather conditions, relations between the space weather parameters and their effect on the stratospheric ozone are presented in section 4. The atmospheric modes are described in section 5. Results of the analyses of the ionosphere-stratosphere coupling by different statistical methods are presented and discussed in section 6. Finally, section 7 contains main conclusions.

## 2 Data

All data series used in this analysis (except the CR series) start on 1 July 2012 and end on 30 June 2014 and originally are of daily or, when possible, bi-daily (00:00 and 12:00 UTC) time resolution.

### 2.1 Atmospheric data

The following data series were used to characterize atmospheric conditions in the troposphere and lower and middle stratosphere above the Iberian Peninsula (see also detailed descriptions in *Morozova et al.* [2017]).

Altitudinal profiles of atmospheric parameters from the sounding station at Madrid airport (08221, LEMD, 40.50°N, 3.58°W, 633 m asl) are from the Integrated Global Radiosonde Archive (IGRA) database. Each of the observed profiles was re-scaled to the uniform pressure scale from 930 to 30 hPa,  $\Delta p = 10$  hPa (91 levels). Two meteorological parameters were analyzed in this paper: the geopotential height of a specific pressure level (*gph*) and the air temperature at this level (*T*). The *T* and *gph* profiles were extended up to the 10 hPa level (resulting in 93 pressure levels total) using the satellite data from the Modern-Era Retrospective Analysis for Research and Applications (MERRA) and the Aqua AIRS Level 3 Daily Standard Physical Retrieval (AIRS+AMSU), AIRX3STD databases. The time variations of the original *T* and *gph* altitudinal profiles can be found in Fig. 1 of *Morozova et al.* [2017]. As deduced from the temperature profiles, the tropopause is located between ~200–150 and ~50 hPa (approximately between 12 and 20 km) depending on the month. In this paper we consider the region between ~50 and ~30 hPa as the lower stratosphere and the region between ~30 and ~10 hPa as the middle stratosphere.

Stratospheric ozone as mole fraction in air measured in the middle stratosphere at 10 hPa levels,  $O_3_{10}$ , averaged over the area of the Iberian Peninsula, is from the AIRX3STD data base.

The QBO phases were defined using the data on the monthly mean equatorial zonal wind components at different stratospheric pressure levels (70–10 hPa) from the Freie Universität Berlin database.

### 2.2 Space weather data

Two parameters were used to analyze the geomagnetic field variations: the global *Dst* index and the locally measured horizontal component of the geomagnetic field measured at the *Coimbra Magnetic Observatory* (IAGA code COI) located in Coimbra, Portugal (40.22°N, 8.42°W, 99 m asl), hereinafter, *COI H*.

The cosmic ray (CR) flux variations analyzed in this study are from the ground *Castilla-La Mancha Neutron Monitor*, *CaLMa* (Guadalajara, Spain, 40.63°N, 3.15°W, 708 m a.s.l.) [Medina et al., 2013]. This station, with a vertical cut-off rigidity  $R_c = 6.95$  GV, gives a direct measurement of the CR arriving to the Iberian Peninsula (see also detailed descriptions in *Morozova et al.* [2017]).



To parameterize the variations of the solar UV radiation we used the *Mg II* composite series [Snow *et al.*, 2014], a proxy for the spectral solar irradiance variability in the spectral range from UV to EUV based on the measurements of the emission core of the Mg II doublet (280 nm). Recently a number of studies [e.g., Danilov, 2017; Chen *et al.*, 2018; Zhang *et al.*, 2018] showed that the widely used F10.7 index is not a good proxy for the solar UV flux variations when variations of ionospheric parameters are studied. Therefore, the *Mg II* series which is based on the direct measurements of the UV solar flux was used instead of F10.7.

The local ionospheric conditions were characterized by the total electron content (TEC) values provided by the *Ebro Observatory*, Spain (40.8°N, 0.5°E, 50 m asl). The instrument currently installed at the *Ebro Observatory* is the DPS-4D ionospheric sounder and the measured parameter is  $f_0F2$ . The altitude profiles of electron density are calculated from the ionograms, and the integration of these electron profiles up to 1000 km height gives the values of a so called TEC without plasmaspheric contribution. Since  $f_0F2$  is used to calculate TEC, these parameters are highly correlated as can be seen in Fig. S1 in the Supporting Information.

### 3 Methods

#### 3.1 Preprocessing and decomposition

The data sets used in this study were prepared using procedures explained in detail in Morozova *et al.* [2017]. In short, the gaps in the data series were linearly interpolated whenever necessary, and the altitudinal profiles of the atmospheric parameters were rescaled to the uniform pressure scale. The annual cycles were removed from the analyzed series (except the CR and Dst series) to produce the *noAC* series [see Morozova *et al.*, 2017]. The *Smoothed* series (for all parameters) were obtained by using a decomposition procedure named seasonal-trend decomposition based on LOESS (STL). This method is described in detail in Cleveland [1979], Cleveland and Devlin [1988], and Cleveland *et al.* [1990]. It allows one to decompose a series into three additive components: a long-term Trend, a Cyclic component with a predefined "period" and a Residual component. The STL procedure can be viewed as a filter that distributes the variations with different periods into three "channels". Those with periods close to the predefined "period" are included in the Cyclic component. The variations with longer periods are filtered into the Trend component, and the rest is regarded as the Residuals. The choice of the "period" values is defined by series' properties and filtering purposes. In this study we used STL to smooth the original series removing short-term variations with characteristic periods shorter than 1-1.5 weeks.

The modes of the variability of atmospheric parameters were extracted by the principal component analysis (PCA) applied both to the *noAC* and *Smoothed* series. To extract the coupled variability of the atmospheric parameters a singular value decomposition of the coupled fields (hereafter "cSVD"), an extension of the PCA, was used. Each of the extracted mode is characterized by the pair of a time varying principal component (PC) and a spatially (here, with altitude) varying empirical orthogonal function (EOF). Further, each mode is reconstructed using the corresponding PC and EOF components to obtain time series of  $T$  and  $gph$  at different pressure levels. The first mode (mode 1) is thoroughly analyzed in Morozova *et al.* [2017] and briefly described in sec. 5.1. The detailed analysis of the second mode (mode 2) is presented in sec. 5.2 and 6.

#### 3.2 Correlation analysis

Similarities between the variations of the analyzed parameters were tested using the Pearson correlation coefficients,  $r$ , that test linear relations between analyzed variables. The correlation coefficients for the *Smoothed* series were computed removing the first and the last

month of the selected time period to avoid uncertainty that could arise from the smoothing. The significance of the correlation coefficients was estimated using the Monte Carlo approach with artificial series constructed by the two following methods: the “phase randomization procedure” [Ebisuzaki, 1997] for the *noAC series* and the “bootstrapping with moving blocks” randomization procedure [Künsch, 1989; Lahiri, 1999] for the *Smoothed series*. The obtained statistical significance ( $p$  value) takes into account the probability of a random series to have the same or higher absolute value of  $r$  as in case of a tested pair of the original series.

### 3.3 Wavelet analysis

The wavelet analysis was used to inspect the evolution of periodicities existing in a data set at different times. The wavelet cross coherence and phase technique was applied to analyze the coherence of a pair of data series, its evolution and the corresponding phase lag between the series. The results are visualized as time-frequency spectra where the powers are represented by different colors (corresponding color map is shown nearby each spectrum). The statistical significance of the computed powers is calculated against the red-noise background. Statistically significant zones of the spectrum (we use the 95% significance level) are contoured by black lines. An influence of boundary effects is taken into account: one should trust only the results inside the so-called “*cone of influence*”. On the wavelet coherence plots the phase relation between the two analyzed data sets – phase lags – are visualized by arrows. If an arrow is directed from left to right then the data sets are in phase, if from right to left they are in anti-phase, if from top to bottom – the first data set leads the second one in quarter of corresponding period. The detailed description of these methods can be found, e.g., in *Torrence and Compo* [1998] and *Maraun and Kurths* [2004]. Please note that since we used the bi-daily data series the “period” on the wavelet and wavelet cross-coherence spectra is in half-days (i.e. “period = 32” means “period = 16 days”).

### 3.4 Convergent cross-mapping analysis

While correlation and wavelet cross-coherence analyses are useful tools in detecting similarities in the time-variations of different parameters, nothing can be said with certainty about the causality or direction of the forcing (if any exists) of the analyzed parameters. Other methods are needed to distinguish causality from spurious correlation of parameters characterizing such dynamical systems as atmosphere. One of such power tool is the convergent cross mapping (CCM). This method is based on empirical dynamics [Sugihara *et al.*, 2012 and references therein] and Takens' theorem [Takens, 1981], which states that the essential information of a multidimensional dynamical system is retained in the time series of any single variable of that system [Tsonis *et al.*, 2015]. The procedure of the CCM analysis allows to detect if the analyzed parameters belong to the same dynamical system or not and, further, to estimate the strength and direction of the causal link. The CCM methodology is thoroughly described in *Sugihara et al.* [2012] and *Tsonis et al.* [2015 and 2018]. Here we give only a short summary.

For a pair of analyzed parameters (e.g.,  $X$  and  $Y$ ), the causation between the series is analyzed comparing the similarity between the original series and the so-called “shadow manifolds”  $M_Y$  and  $M_X$  (correspondingly) constructed from lagged coordinates (nonlinear state space reconstruction) of the corresponding ( $Y$  and  $X$ , respectively) time series. It is also called a “cross mapping of  $X$  by using  $M_Y$ ” or  $X|M_Y$  and “cross mapping of  $Y$  by using  $M_X$ ” or  $Y|M_X$ . The basic concept of CCM is that a unilateral causation (e.g.,  $X$  drives  $Y$ ) results in a possibility to estimate  $X$  from  $Y$ , but not  $Y$  from  $X$  [Schiecke *et al.*, 2015]. For a bilateral causation with different strengths of the causal link, the quality of the estimations depends on the strength of such link. This quality, or predictive skill, is estimated by a series of

correlation coefficients, denoted here as  $\rho(X|M_Y)$  and  $\rho(Y|M_X)$ , between the “inputs” (X or Y) and “predictions” ( $M_Y$  or  $M_X$ , correspondingly) for data sets with gradually increasing length (length of library, L). If the skill increases with L, a direct or indirect causal effect of X on Y (or vice versa) can be inferred. Since CCM uses nonlinear state space reconstruction, the causal relations detected by it can be nonlinear too (in contrast to the Pearson correlation discussed in sec. 3.2).

The essential part of CCM is the analysis of the convergence of the  $\rho$  series with the increasing L [Sugihara *et al.*, 2012]. As was shown in Mønster *et al.* [2017], the good fit of the converging  $\rho(L)$  series by an exponential function should be used as an indicator that CCM is applicable to the data set in question, and that its results are reliable.

If only  $\rho(X|M_Y)$  converge and  $\rho(Y|M_X)$  does not (meaning that X can be well reconstructed from Y but not vice versa) then it means that the Y series contains information on X, and X forces variations of Y. When both  $\rho$  series converges, it is possible that those parameters are affecting each other more or less equally or they are forced by a third agent [see examples in Sugihara *et al.*, 2012]. The statistical significance of the  $\rho$  series can be tested using the Monte-Carlo approach and the phase randomization procedure (see sec. 3.2).

CCM was already successfully applied to the analysis of causal relations in biological [Sugihara *et al.*, 2012] and atmospheric [van Nes *et al.*, 2015] systems as well as to test the CR and climate relations [Tsonis *et al.*, 2015]. Here we applied the CCM analysis [using the R implementation by Ye *et al.*, <https://cran.r-project.org/package=rEDM>] to test the causal nature of relations between the atmospheric and space weather parameters detected by the correlation analyses (see sec. 5).

Please note that only non-autocorrelated series can be used as the input data sets for CCM [Tsonis *et al.*, 2015]. Therefore, only *noAC* series were submitted to the CCM analysis. Also, the first time derivative of the *Mg II noAC* series was used in the CCM analyses instead of the original series [see discussion in Tsonis *et al.*, 2018 and references therein].

#### 4 Space weather parameters

The *noAC* and *Smoothed COI H*, *O<sub>3 10</sub>*, *TEC* and *Mg II* series are shown in Figs. 1a, 1b, 1d and 1e, respectively. The *TEC* and *O<sub>3 10</sub>* series are, as expected, statistically significantly correlated with *Mg II* (Table 1) both for the whole length of the series and for the cold seasons only (from November to April). Other pairwise correlation coefficients are weak and/or statistically insignificant (not shown).

The wavelet analysis of the *COI H*, *TEC* and ozone series show persistent variations with periods of ~2-4 months and transient variations with periods ~1-4 weeks. The *Mg II* series show periodic variations close to the period of solar rotation (~27 days) overlaid by short-term variations. Corresponding spectra for the *noAC* series can be found in the Supporting Information (Fig. S2). The wavelet cross-coherence analysis shows that *TEC* variations are in phase with variations of *Mg II* with periods close to 27 day-long solar rotation period and its 2<sup>nd</sup> and 3<sup>rd</sup> harmonics (see Fig. S3b in the Supporting Information). The relations between the *TEC* and *COI H* series are more complex. Generally, these parameters are directly in the anti-phase. However, for some periods and during some time intervals (see wavelet cross-coherence spectrum in Fig. S3e in the Supporting Information) there are time lags between the variations of *TEC* and *COI H*. These lags can result from the ionosphere-magnetosphere coupling: during some time intervals the ionosphere is affected by geomagnetic storms generating a signal with specific frequencies; during other time intervals there is an opposite forcing when ground measured geomagnetic field has a strong components generated in ionosphere. Please also note that the *Sq* variation was not



specifically removed from the *COI H* bi-daily series during the pre-processing, but the *TEC* series were smoothed to remove 1 day periodicities. On the other hand, the variations with  $\sim 1$  day period are absent in the *Smoothed* series.

**Table 1.** Correlation coefficients between *Mg II*, and *TEC* and *O<sub>3 10</sub>* series for the *noAC*, *noAC* smoothed by 3-points adjacent averaging and *Smoothed* series for data sets of different length: whole series, only winter seasons (from November to April) of 2012-2013 and 2013-2014. Only correlation coefficients  $|r| \geq 0.2$  are shown. Correlation coefficients without *p values* (shown in parentheses) are statistically insignificant.

	whole series	eQBO winter (Nov12 - Apr13)	wQBO winter (Nov13 - Apr14)
<i>(A) no AC</i>			
TEC vs Mg II	0.37 (<0.01)	0.43 (<0.01)	0.29 (<0.01)
O <sub>3 10</sub> vs Mg II		0.20	
<i>(B) noAC (adj. aver. 3 pts.)</i>			
TEC vs Mg II	0.5 (<0.01)	0.57 (<0.01)	0.39 (<0.01)
O <sub>3 10</sub> vs Mg II		0.26 (0.12)	
<i>(C) Smoothed</i>			
TEC vs Mg II	0.50 (0.01)	0.45	0.88 (0.03)
O <sub>3 10</sub> vs Mg II		0.38	-0.62

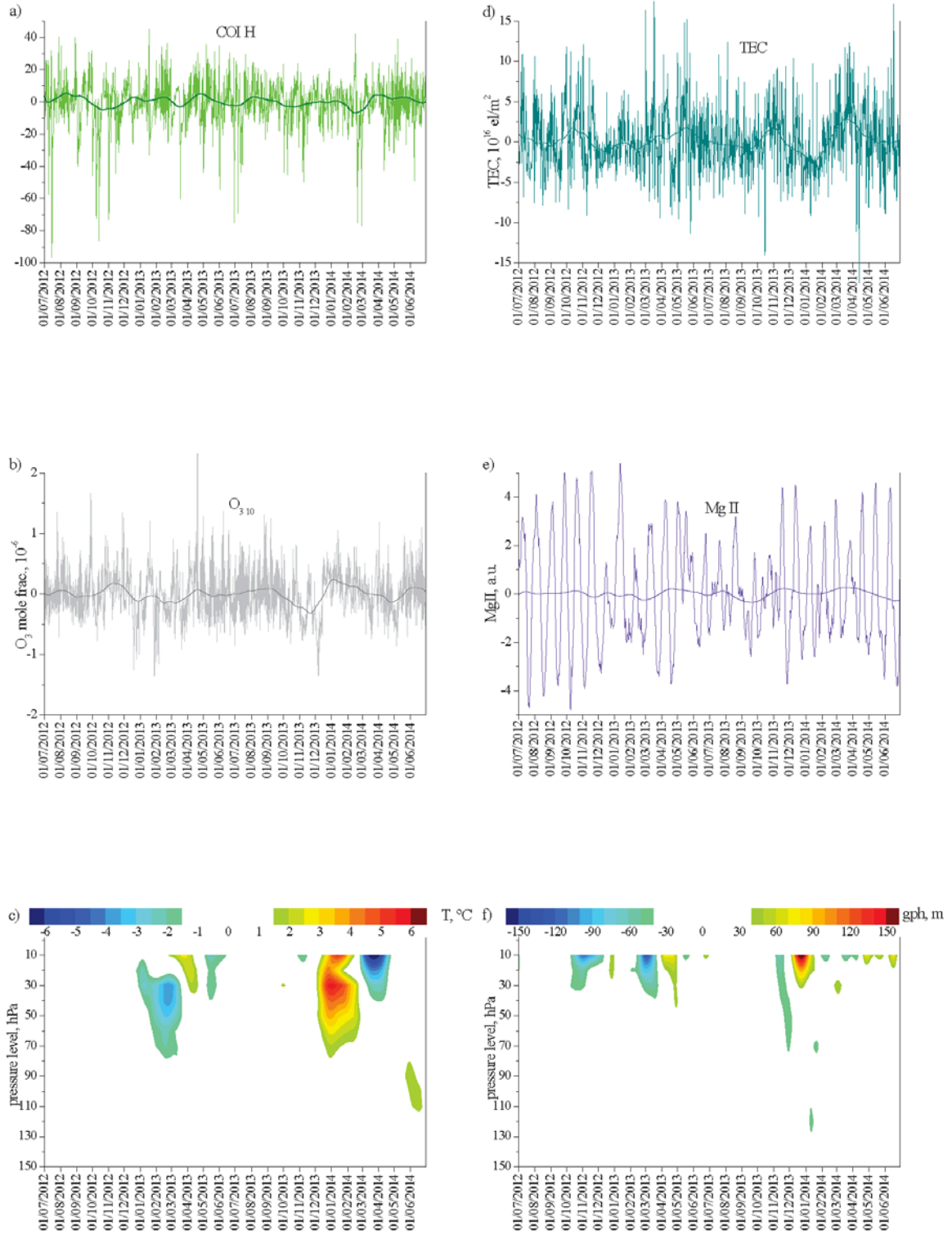


**Figure 1.** Top: *noAC* (thin line) and *Smoothed* (thick line) series of  $COI\ H$  (a),  $O_3$  (b),  $TEC$  (d) and  $Mg\ II$  (e). Bottom: Altitudinal profiles (colors) of the *Smoothed* series of  $T$  (c) and  $gph$  (f) between 100 and 10 hPa with subtracted mode 1 (see sec. 5.1).

The CCM analysis of the causal links between *TEC* and *Mg II* done for two winter seasons shows statistically significant influence of the *Mg II* variations on *TEC* during the *eQBO/SSW* winter. For the *wQBO* winter the prediction skill  $\rho(\text{Mg II}|\text{M}_{\text{TEC}})$  is higher than  $\rho(\text{TEC}|\text{M}_{\text{Mg II}})$ , plus the correlation coefficient between the  $\rho(\text{Mg II}|\text{M}_{\text{TEC}})$  series and its exponential fit ( $r = 0.71$ ) is higher than corresponding correlation coefficient for  $\rho(\text{TEC}|\text{M}_{\text{Mg II}})$  ( $r = 0.45$ ). Corresponding plots can be found in the Supporting Information (Fig. S3a and S3c). Therefore, we can conclude that *Mg II* still influences the *TEC* variations; however, the statistical significance of this link is lower than 95%. These findings can be explained by the stronger influence on the ionospheric *TEC* of other forcings: geomagnetic storms and upper atmosphere dynamics/composition.

The CCM analysis of the causal links between *TEC* and *COI H* shows that these parameters are coupled and/or under effect of an external forcing:  $\rho(\text{COI H}|\text{M}_{\text{TEC}})$  and  $\rho(\text{TEC}|\text{M}_{\text{COI H}})$  are of the same amplitude and are well fitted by the exponent ( $0.88 \leq r \leq 0.99$ ). Corresponding plots can be found in the Supporting Information (Fig. S3d and S3e). These ambiguous results are probably due to the mutual influence of the ionospheric electric and the geomagnetic field. Geomagnetic disturbances affect ionosphere while the ionospheric daily currents and irregular disturbances produce magnetic field variations measured at the ground level. It is possible that the *COI H* and *TEC* series need specific pre-processing to disentangle common variabilities (e.g., separation to the quiet and disturbed components or filtering of signals with specific periods) for a successful CCM analysis.

The wavelet cross-coherence and CCM analyses applied to the study of the relations between the solar UV radiation (*Mg II*) and the middle stratospheric ozone (*O<sub>3 10</sub>*) show that some part of the ozone variations during winter seasons are caused by the solar UV, but there are also other forcings (most probably, atmospheric chemistry and dynamics) strongly affecting ozone content in the middle stratosphere and decreasing the statistical significance of the CCM results (please see Supporting Information Fig. S4).

## 5 Atmospheric modes

### 5.1 Mode 1

The first mode of the *T* and *gph* variations is thoroughly described in *Morozova et al.* [2017]. It is defined as PC1/EOF1 obtained both in the PCA and cSVD analyses. It explains a significant part of the variability of the parental series (67–79%). Here we give only a brief description of the found relations with space weather parameters. The first mode of the regional (Iberian Peninsula) atmospheric variability is related to the hemispheric-scale circulation forced by the polar vortex conditions and SSW events. The *T* and *gph* variations associated to this mode correlate with the lower stratospheric ozone *O<sub>3 50</sub>* and anti-correlate with the CR flux variations. It was also found that the strength of these correlations depends on the QBO phase (and/or existence or absence of SSW) and, as a consequence, on the blocking or strengthening of the meridional circulation in the Northern Hemisphere stratosphere. We proposed two mechanisms that can explain the found co-variability. The first one is based on the effect of CR particles on the composition of the upper and middle atmosphere (*NO<sub>x</sub>* and *HO<sub>x</sub>* species) and, consequently, on the ozone content in the polar regions and on the polar vortex conditions that, through the coupling between the troposphere and stratosphere in the middle and high latitudes, may affect atmosphere even at ~40°N. Another reason for the co-variability of the atmospheric parameters and CR is the so-called atmospheric effect (dependence of the ground-measured neutron monitor data on the atmospheric temperature and pressure) that is not fully accounted for by the standard procedure of pressure correction. This assumption is based on the fact that the highest

correlation coefficients between the CR and the  $T$  and  $gph$  series were obtained for the altitudes of  $\sim 100$ – $200$  hPa or  $\sim 12$ – $16$  km, the region where most of the secondary neutrons are produced. Unfortunately, the time scale of the analyzed variations (weeks to months) does not allow discriminating between these two mechanisms.

Since the mode 1 of the  $T$  and  $gph$  variations is analyzed in *Morozova et al.* [2017], here the *Smoothed*  $T$  and  $gph$  series are shown with mode 1 subtracted (Figs. 1c and 1f, respectively). These plots can be compared with Figs. 2b and 2d in *Morozova et al.* [2017], respectively.

## 5.2 Mode 2

In this paper we present the analysis of the variation of the second atmospheric mode. It consists of the followings PCs/EOFs. For the *noAC* series: PC2/EOF2 from the PCA analysis of the  $T$  series and PC4/EOF4 from the PCA analysis of the  $gph$  series, and PC4/EOF4 from the cSVD analysis of the  $T$  and  $gph$  series. For the *Smoothed* series: PC4/EOF4 from both PCA and cSVD analysis of both the  $T$  and  $gph$  series. This mode explains  $\sim 6$ – $15\%$  of the temperature variations,  $\sim 2.5\%$  of the  $gph$  variations, and  $\sim 3.7\%$  of the common variability of the  $T$  and  $gph$  fields. Figure 2 shows reconstructed variations of the  $T$  and  $gph$  mode 2 as color time-altitude plots and the corresponding PCs (for the *Smoothed* series) as lines with symbols (Figs. 2a and 2c). These plots can be compared with Figs. 5a and 5c, respectively, in *Morozova et al.* [2017] showing variations related to the mode 1. The PCs obtained for the *noAC*  $T$  series are shown in Fig. 3 (winter seasons only).

The mode 2 is located in the lower and middle stratosphere. The highest amplitudes related to this mode are seen above  $\sim 70$  mbar level for the  $T$  variations and above  $\sim 30$  mbar for  $gph$ , as is seen in Figs. 2b and 2d. The mode 2 is a winter mode: its PCs have highest amplitudes between November–December and April, as shown in Figs. 2a and 2c. Wavelet analysis of the mode 2 *noAC* PCs shows statistically significant variations with period  $\sim 4$ – $6$  months and a more short-living variability with periods  $\sim 1$ – $5$  weeks, mostly during winter periods and especially during the *eQBO/SSW* winter. Corresponding spectra can be found in the Supporting Information (Fig. S5).

When compared to space weather and ozone parameters the mode 2 shows statistically significant correlations with the  $TEC$  and  $O_{3\ 10}$  series, as shown in Fig. 4. On the whole, the mode 2 anti-correlates with  $TEC$  and correlates with  $O_{3\ 10}$  (Fig. 4a). Contrary to the mode 1, the mode 2 shows no correlations with  $Dst$  (a global parameter characterizing the geomagnetic field variations comparing to the regional  $COI\ H$ ), but it anti-correlates with  $CR$  when only winter periods and smoothed series are taken into consideration (Figs. 4b and 4c).

We presume that at least part of the variations of this atmospheric mode, especially during the winter season with lower level of insolation, may result from the stratospheric-ionospheric coupling. This hypothesis is tested using different mathematical approaches in sec. 6.

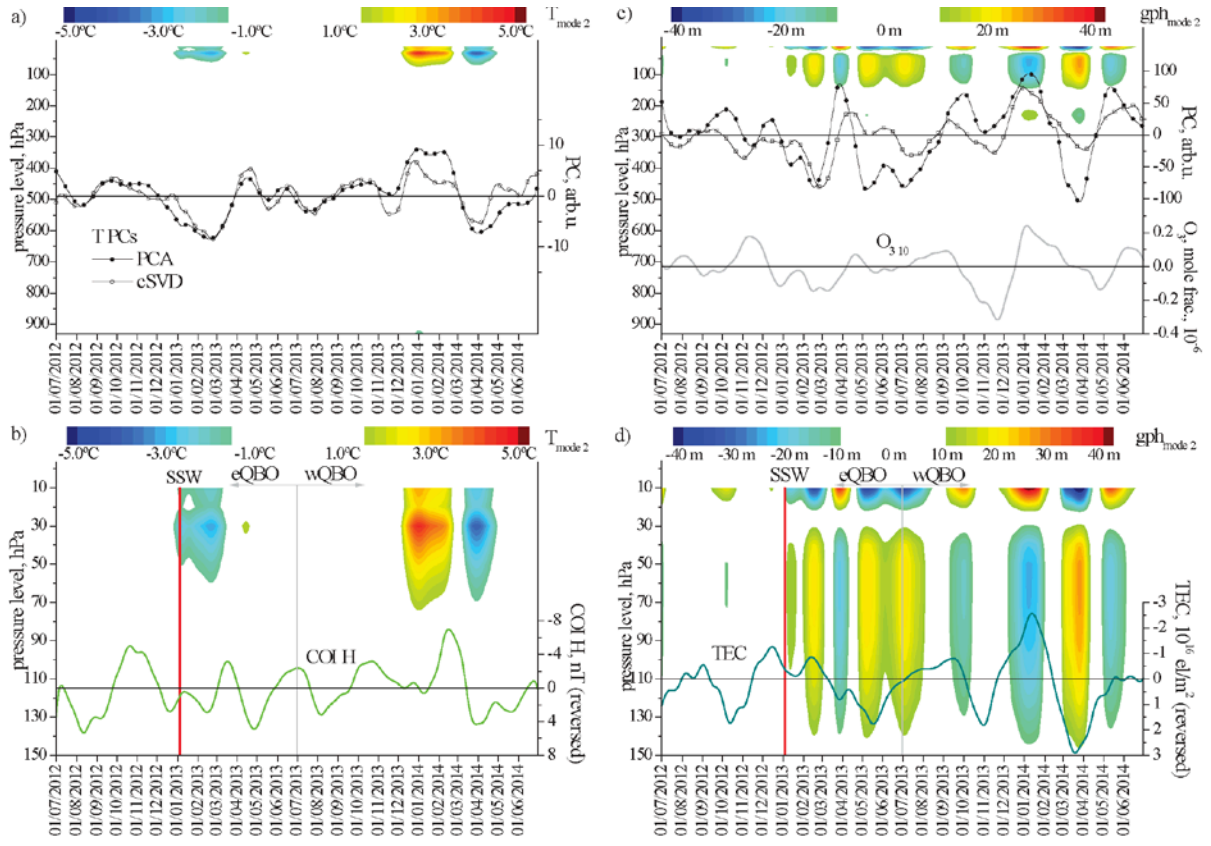


**Figure 2.** Reconstructed variations of the *Smoothed T* (930-10 hPa - **a**, and 150-10 hPa - **b**) and *gph* (930-10 hPa - **c**, and 150-10 hPa - **d**) series related to the mode 2 (colors) together with corresponding PCs of the *Smoothed* series: **a** and **c**, lines with filled (PCA) and open (cSVD) symbols. Also shown: *Smoothed COI H* (**b**, green line),  $O_3\ 10$  (**c**, light grey line) and *TEC* series (**d**, dark cyan line). On **b** and **d** the vertical red lines mark SSW event and grey lines separate  $eQBO$ /SSW and  $wQBO$  epochs.



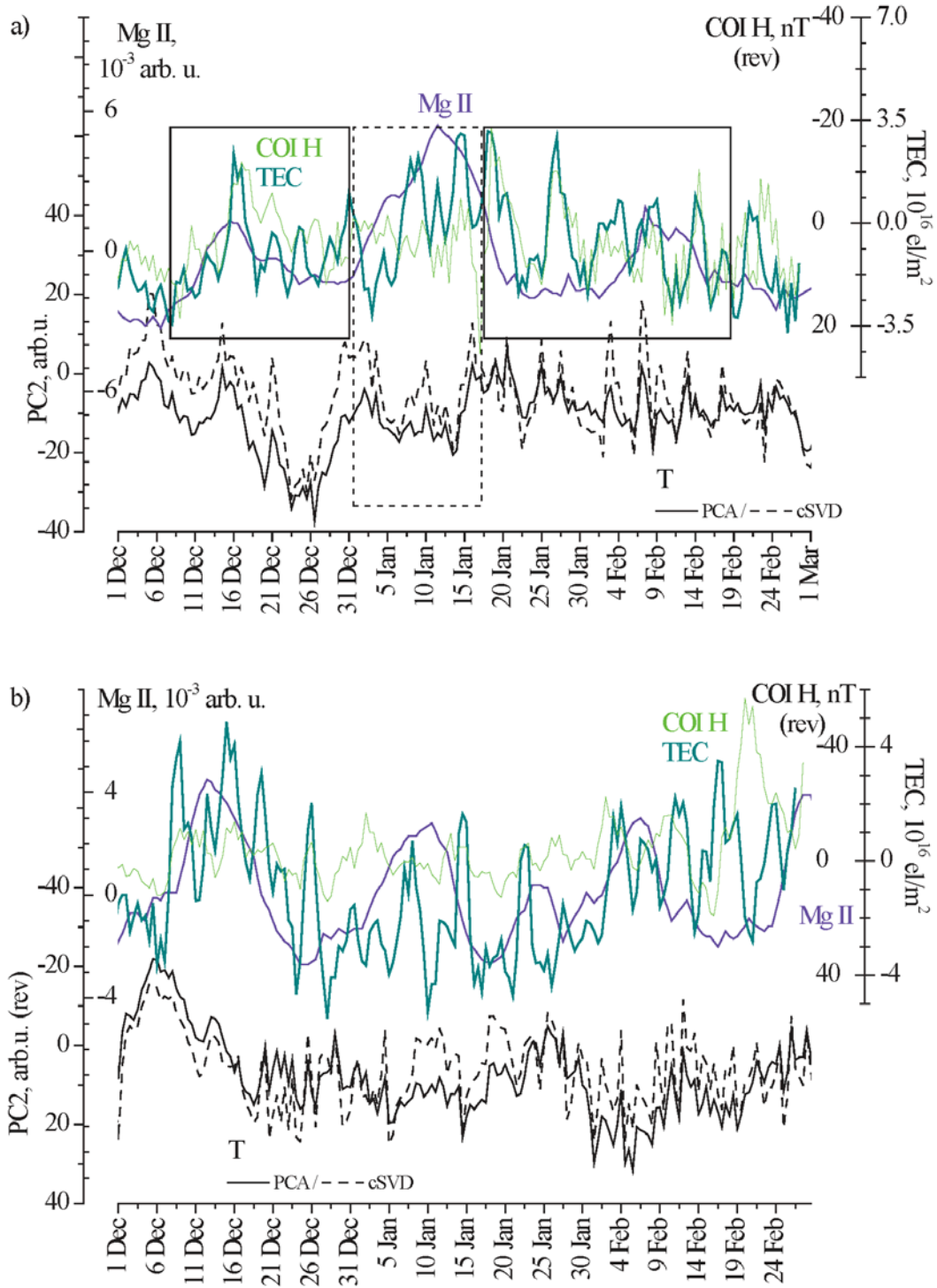


**Figure 3.** Variations of the noAC TEC (dark cyan lines), Mg II (violet lines), COI H (green lines) series and the noAC T PC2 (black solid/dashed lines for PCA/cSVD). All series are smoothed by the 3-days adjacent averaging. Please note reversed Y-axes for COI H. (a) Between December 2012 and February 2013. Black solid line rectangles show periods of coupled geomagnetic and ionospheric variations and black dashed line rectangle shows pre-SSW and SSW period. (b) Between December 2013 and February 2014. Please note reversed Y-axes for PC2s.

## 6 Stratosphere-ionosphere coupling as seen by different methods

Figure 3 shows winter variations of the temperature mode 2 (both from the PCA and cSVD analyses) together with variations of the ionospheric *TEC* and its main external forcings – solar UV flux (*Mg II*) and geomagnetic field (*COI H*). All *noAC* series are smoothed by the 3 points adjacent averaging. As one can see, the solar UV changes, mostly with ~27 days periodicity, affect the average level of *TEC*. The same can be deduced from the wavelet cross-coherence analysis (Fig. S3b). The short-term variations of *TEC* are in a good agreement with changes of the *COI H* – these two series anti-correlate (please note reversed Y-axes for *COI H* in Fig. 3) but the values of the statistical significance of the correlation coefficients are low (not shown here).

The interesting feature of the *TEC* variations that can be deduced from Fig. 3 is that during both winters *eQBO/SSW* and *wQBO* the *TEC* series generally follows the changes of the UV solar flux (*Mg II* series) and the geomagnetic field (*COI H* series) during the whole December – February time intervals. For example, during the *eQBO/SSW* winter small geomagnetic disturbances (~30-50 nT) around January 15-16, 2013 and around January 26, 2013 coincide with increased *TEC* values. However, the sharp increase of *TEC* between December 26, 2012 and January 14, 2013 (marked in Fig. 3a by the dashed line rectangle) is hardly explained by geomagnetic field variations, and the growing trend of UV solar flux is expected to cause only a global increase of the *TEC* level. This time interval corresponds to the pre-SSW and SSW conditions related to the SSW event started on January 6, 2013. Following *Goncharenko et al.* [2013] and *Chen et al.* [2016], we can attribute these changes in *TEC* observed before and during the SSW event to the stratosphere-ionosphere coupling.

The stratospheric conditions do not affect the ionospheric *TEC* directly, but, most probably, through a change of the conditions for the gravity waves/tides upward propagations. When such waves/tides reach the mesosphere and thermosphere, they interact with waves and tides in the upper atmosphere changing conditions in the neutral and, as a consequence, ionized components of the ionosphere [*Laštovička et al.*, 2012]. Since the conditions for propagation of these waves and tides depends on the QBO phase and/or existence of the SSW events, the comparison of the results obtained for the *eQBO/SSW* and *wQBO* winters can allow one to deduce the existence and significance of the stratospheric-ionospheric coupling during the analyzed time interval over the Iberian Peninsula. In sec. 6.1-6.3 we present the analysis of the winter season variations of the ionospheric and stratospheric parameters and confirmations of their couplings obtained by the correlation, wavelet cross-coherence and CCM analyses.

We have to mention that while *T* and *gph* mode 2 PCs are very similar (Figs. 2 and 3) and coupled (especially, the cSVD PCs), there is no strict similarity of the performances of the *T* and *gph* mode 2 PCs in the correlation, wavelet and CCM analyses. The explanation is, probably, in the spatial distribution of the *T* and *gph* mode 2: while the *T* mode 2 has maximum around 50-20 hPa, the *gph* mode 2 reaches the highest amplitude above 30 hPa level with a see-saw like pattern (variations at 150-30 hPa oppose one at 30-10 hPa level, Fig. 3).

### 6.1 Correlation analysis

First of all, the sign of correlation coefficients between the PCs of *T/gph* and the *O<sub>310</sub>* series is the same for both winters, but the highest correlation coefficients are obtained for the *wQBO* winter (Figs. 4b and 4c). Same can be said about relations between *TEC* and *Mg II* (Table 1) which is expected since solar-magnetosphere-ionosphere interactions do not depend on the atmospheric circulation.

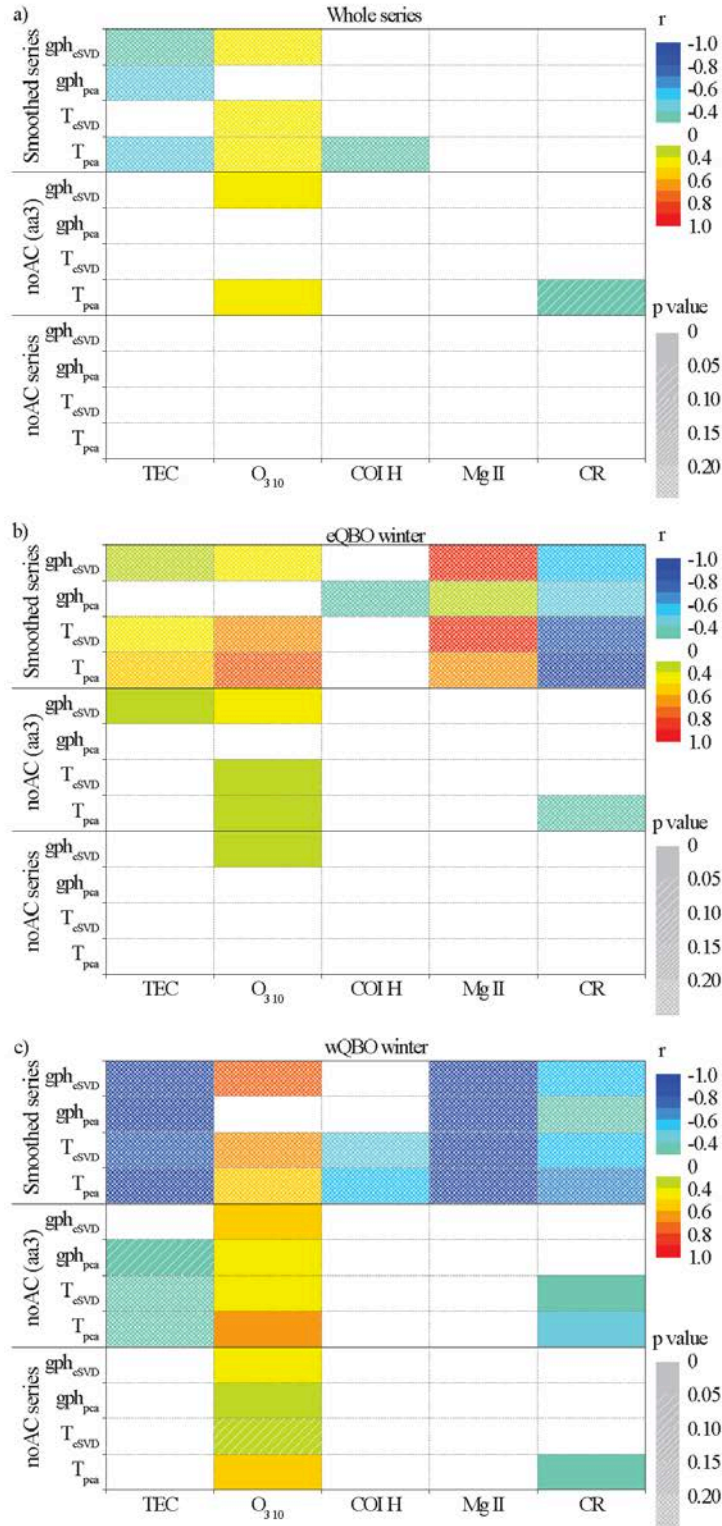


**Figure 4.** Correlation coefficients between the mode 2 PCs (PCA and cSVD) of  $T$  and  $gph$ , and space weather ( $TEC$ ,  $COIH$ ,  $CR$  and  $Mg II$ ) and ozone parameters: (a) whole series, (b)  $eQBO/SSW$  winter, (c)  $wQBO$  winter. Correlation coefficients are shown as colors and corresponding p values are shown as shading (less shading corresponds to lower p values meaning higher statistical significance). Correlation coefficients are calculated for the *noAC*, *noAC* series smoothed by the 3-points adjacent averaging and the *Smoothed* series.

Change of the sign of the correlation coefficients calculated for the *eQBO/SSW* and *wQBO* winters was found for the following pairs of parameters: PCs of *T/gph* vs *TEC* (Figs. 4b and 4c) and *Mg II* vs *O<sub>3 10</sub>* (Table 1). For the *eQBO/SSW* winter the mode 2 tends to correlate with *TEC*, whereas for the *wQBO* winter there is a strong anti-correlation (please compare Figs. 4b and 4c). Please note that the statistical significance of the correlation coefficients of the *Smoothed* series is low due to the high level of the autocorrelation of the smoothed series. These differences between the *eQBO/SSW* and *wQBO* winters can be partly explained by the increased solar and geomagnetic activity during the second winter season (corresponding to the higher second solar activity peak during the solar maximum): higher values of the UV flux, more flares, CMEs and geomagnetic storms can be deduced from Figs. 1a and 1e [see also Table S1 in *Morozova et al.*, 2017]. Nonetheless, it seems that the intra-atmospheric relations (e.g., between temperature and pressure fields and *TEC*) are QBO-dependent and controlled by the atmospheric dynamics and conditions for the waves/tides propagation. On the other hand, these two winters are different by not only the QBO phase but also by the appearance/absence of the SSW event. Therefore, it is possible to attribute the change of the sign of the correlation between the mode 2 and *TEC* to the influence of SSW that is known to affect the whole Northern hemisphere and conditions for the waves/tides propagations (see sec. 1).

## 6.2 Wavelet cross-coherence analysis

The wavelet cross-coherence analysis of the variations of the mode 2 *noAC* PCs vs *TEC* and vs *O<sub>3 10</sub>* *noAC* series confirms results obtained by the correlation analysis for the *eQBO/SSW* and *wQBO* winters (see Figs. 5b and 5e, and corresponding Figs. S6a and S6b). In particular, there is a clear inter-winter difference in the cross-coherence spectra for the mode 2 vs the *TEC* series. During the *eQBO/SSW* winter (white rectangles “1”) there are (almost) in-phase variations between the mode 2 PCs and *TEC* with periods of ~8-16 days (compare to Fig. 4b). On contrary, during the *wQBO* winter (white rectangles “2”) there are anti-phase variations between the mode 2 PCs and *TEC* series at periods of ~3-4 months (compare to Fig. 4c). The analysis of the relations between the atmospheric parameters and the ozone (Figs. S7 and S8 in the Supporting Information) shows that all mode 2 PCs are in-phase with variations of the *O<sub>3 10</sub>* series at periods longer than 4 months throughout a year and at periods ~3-4 weeks during winter seasons (similar to what is shown in Figs. 4b and 4c).

## 6.3 Convergent cross mapping

Correlation and wavelet analyses show similarities between the PCs for the *T/gph* mode 2 and the *TEC* and *O<sub>3 10</sub>* series. To study the possible causal relations between these parameters the CCM method was used. Results of the CCM analysis are shown in Fig. 5 for the mode 2 PCs vs *TEC* and in Fig. S7 for the mode 2 PCs vs *O<sub>3 10</sub>*. They represent changes of the prediction skill  $\rho$  (correlation coefficients between the original series and the CCM reconstruction) with increase of the library length  $L$  shown as percent of the length of a data set submitted to the CCM analysis. Color-shaded areas of the corresponding plots show 95% significance level obtained using the Monte-Carlo simulations.

The CCM analysis for the two winter seasons (Figs. 5a vs 5c and Figs. 5d vs 5f) shows that the *T* and *gph* series are well reconstructed from the *TEC* series for the *eQBO/SSW* winter: the  $\rho(T|M_{TEC})$  and  $\rho(gph|M_{TEC})$  converge and have statistical significance  $> 95\%$  (Figs. 5a and 5d); they are also well fitted by the exponential function ( $0.97 \leq r \leq 0.99$ ). For the *wQBO* winter the CCM analysis show no causal link between variations of the mode 2 and *TEC* except for the PCA PC for the *gph* series (Fig. 5f): in this particular case  $\rho(gph|M_{TEC})$  is significantly higher than  $\rho(TEC|M_{gph})$  and well fitted by the exponent ( $r = 0.94$ ), but statistical significance of this result is low.



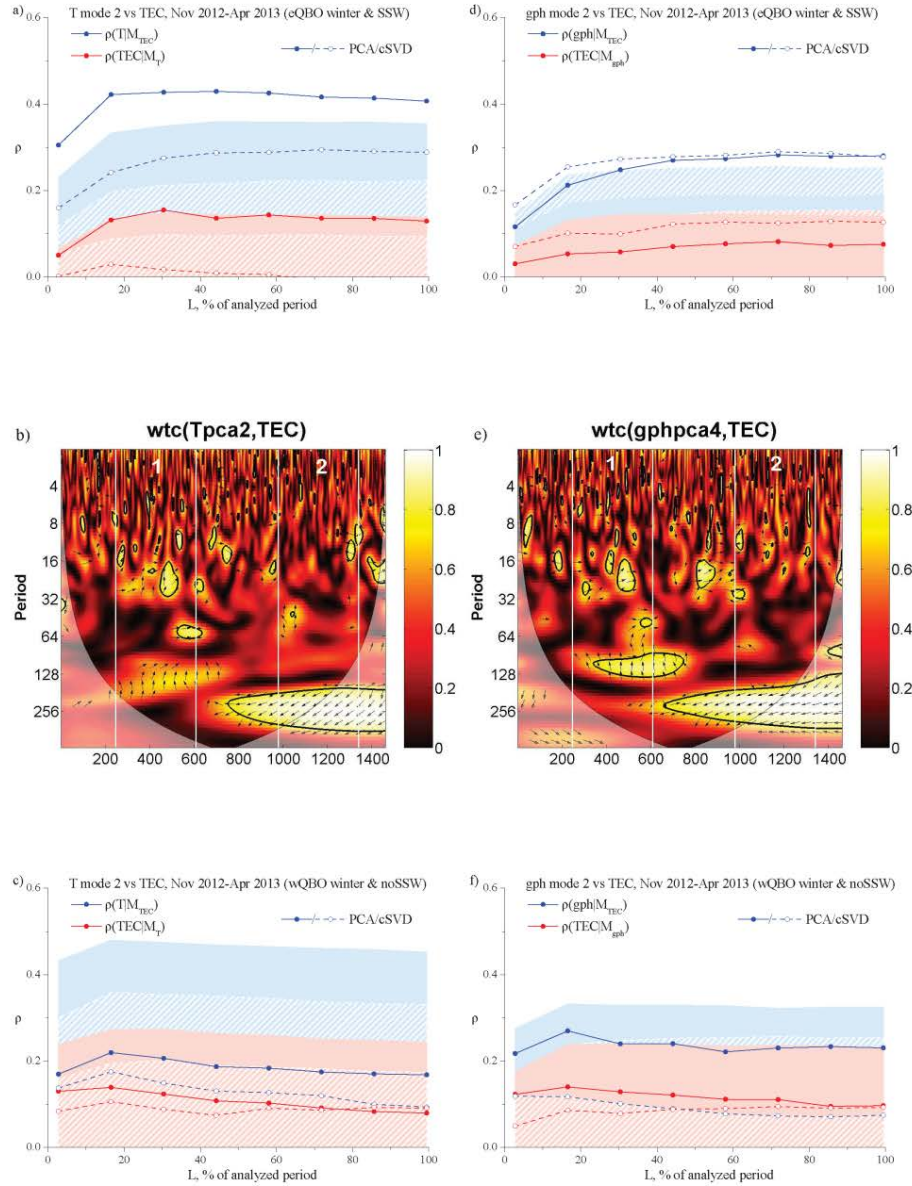


**Figure 5.** Left: Results of the CCM analysis of the *TEC* vs PCs of the *noAC* *T* mode 2 (PCA—solid lined with solid dots, and cSVD — dashed lines with open dots) for the *eQBO/SSW* (a) and *wQBO* (c) winters. The skill of cross-map estimates, indicated by the correlation coefficient ( $\rho$ ), varies with the library length  $L$  shown as a percentage of the analyzed time interval (362 points). Blue lines are reconstructions of *TEC* from *T* PCs, red lines are reconstructions of *T* PCs from *TEC*. Shaded areas show 95% significance level (solid colors for PCA and colors with white stripes for cSVD). Wavelet cross-coherence spectrum (b) for the whole time interval (1460 pts, counted in 0.5\*day starting from July 1, 2012) between *T* PCA PC2 and *TEC*. White rectangles mark *eQBO/SSW* ("1") and *wQBO* ("2") winters. Statistically significant values are inside the black contours. Area outside of cones of influence is shaded. The period is in 0.5\*day (e.g., period = 32 equals to the period of 16 days). See section 3.3 for explanations on the arrows directions. Right: same as left but for *gph* PCs.



The CCM analysis of the relations between the  $T$  mode 2 and the ozone series shows that  $T/gph$  and  $O_{3\ 10}$  affect each other: both  $p(T|O_{3\ 10})$  and  $p(O_{3\ 10}|T)$  series converge. This is to be expected since the ozone heats the stratosphere absorbing solar UV light, but an increase of the temperature in the presence of some atmospheric constituents (like  $NO_x$  species) can result in an intensification of the ozone destruction [Flury *et al.*, 2009]. Besides, both temperature and ozone content are affected by the air masses circulation which, in turn, is affected by the QBO phase, season and features of the global atmospheric dynamics. For example, at the latitudes of the Iberian Peninsula the proportion of the ozone originated at higher/lower latitudes changes with season [Grewe, 2006]. Also, the position of the peninsula (between the polar and subtropical jets, see Mohanakumar [2008]) results in an advection of the polar ozone poor air masses during SSW [Keil *et al.*, 2007] that can be seen as well in Fig. 2c. Previous studies [Randel and Cobb, 1994; Lee and Smith, 2003; Mohanakumar, 2008] also showed the QBO-dependant ozone variations during winter months.

Still, the results of the CCM analysis suggest that during the studied winter seasons the influence of the stratospheric temperature and pressure (atmosphere dynamics) on the ozone content is stronger than the influence of the ozone heating on the stratospheric conditions (see Figs. S7a vs S7c and Figs. S7d vs S7f in the Supporting Information). Also, the results of the CCM analysis for the  $gph$  series have, generally, higher statistical significance. We also note that for the  $wQBO$  winter (without strong perturbations in the Northern Hemisphere atmospheric dynamics associated with SSW) the link between the temperature and the ozone content detected by CCM is more straightforward and statistically significant ( $\geq 95\%$ , see Fig. S7c). The skill  $p(T|M_{O_{3\ 10}})$  is higher and is better fit by the exponential function ( $r = 0.99$ ) than  $p(O_{3\ 10}|M_T)$  ( $r = \sim 0.2$ ). For the  $eQBO/SSW$  winter (Fig. S7a) the influence of the stratospheric temperature on the ozone seems to be weaker.

#### 6.4 Discussion

The results of three different methods and, in particularly, the CCM analysis confirm the hypothesis that the changes of the stratospheric  $T$  and  $gph$  force variations of the ionospheric  $TEC$  during at least the  $eQBO/SSW$  winter. Probably, this forcing can be deduced for the  $gph$  mode 2 for the  $wQBO$  winter as well, but the statistical significance of this result is  $< 95\%$ . One must keep in mind that both the stratospheric temperature and ionospheric  $TEC$  can be affected by the solar UV flares: the former indirectly through the variations of the ozone content and the latter directly through the ionization by the UV light. All this could influence the CCM estimations of the strength and direction of the causal link between the  $T$  and  $TEC$  series.

We assumed that the correlation of the  $T/gph$  mode 2 and the  $TEC$  series is due to the stratosphere-ionosphere coupling, probably through the gravity waves and tides. If this assumption is correct, then the lower statistical significance of the CCM results for the  $wQBO$  winter can result from a lower intensity of the gravity waves during the second winter, as was shown previously in, e.g., Chernigovskaya *et al.* [2015], Yiğit *et al.* [2016] and Solomonov *et al.* [2017]. We found confirmation for this hypothesis in the recently published data by Ern *et al.* [2018]. As one can see in their Figs. 19-20, for the  $40^\circ$  N latitudinal zone the winter 2012-2013 ( $eQBO/SSW$ ) is characterized by an intense and long-lasting (until spring 2013) activity of gravity waves at all analyzed altitudes (from 30 to 70 km). On contrary, the gravity waves activity observed during the winter 2013-2014 ( $wQBO$ ) is restricted to the winter months. The enhancement of variations with periods 8-18 days observed during the  $eQBO/SSW$  winter in the variations of the ozone,  $TEC$  and  $T/gph$  series (“period = 16-36” in Figs. 5b, and Figs. S2c, S6, S7b and S8b in the Supporting Information) can be considered as another confirmation for the proposed hypothesis. Previous studies [e.g., Kazimirovsky, 2003;

*Sridharan*, 2017] found that quasi-periodic oscillations in the ionospheric parameters with periods of 6-16 days may be connected with planetary wave activity in the lower atmosphere. Moreover, [*Sridharan*, 2017] showed that during the SSW 2013 event the planetary waves with periods close to 16 days propagate from high-latitudes toward the equator and interact with the semidiurnal tides there. The time lag between the high and low latitudes is of the order of 3 weeks [see *Sridharan*, 2017]. This time lag is in the agreement with time of appearance in our mid-latitudinal region of the coherent signal in the cross-coherent spectra of *T* mode 2 vs *TEC*: about 1-1.5 weeks after the SSW onset (see Figs. 5b, 5e and Fig. S6). Also, *Pancheva et al.* [2003], *Goncharenko et al.* [2012] and *Jin et al.* [2012] showed that variations with periods 8-12 and 15-18 days are observed during SSW winters in the amplitude modulation of the semidiurnal tide, which is considered to play primary role in the stratosphere-ionosphere coupling during the SSW events [e.g., *Pedatella and Forbes*, 2010; *Goncharenko et al.*, 2012].

## 7 Conclusions

The present analysis of the regional (Iberian Peninsula) atmospheric, ionospheric and geomagnetic parameters during a 2-year time interval (from July 2012 to June 2014) showed the role of the stratosphere-ionosphere coupling in the mutual variations of those parameters. While variations of the ionospheric total electron content (TEC) are expected to be forced by the solar and geomagnetic activity (e.g., UV flares and geomagnetic storms), some of the TEC variations, especially during the winter characterized by a sudden stratospheric warming (SSW) event, are internally forced by the stratosphere-ionosphere coupling mechanisms.

Using the principal component analysis (PCA), we extracted a second mode of the temperature (*T*) and pressure (*gph*) variations located in the low-middle stratosphere (above ~70 hPa pressure level) that co-vary with ionospheric and geomagnetic parameters. This mode (explaining ~6-15% and ~2.5% of *T* and *gph* variations, respectively) is influenced by the global and hemispheric dynamics (QBO and polar vortex conditions) and found to statistically significantly correlate with variations of the middle stratospheric ozone content and ionospheric TEC. Similar variability of the stratospheric and ionospheric parameters was found also by the wavelet cross-coherence analysis.

To analyze the causality of the found correlations we applied the convergent cross mapping (CCM) analysis to our series, and the obtained results seems confirming the causal character of the relations between the variations of the stratospheric (temperature and *gph*) and ionospheric (TEC) parameters. During winter months, and especially during the SSW event in January 2013, the ionosphere above the analyzed region seems to be forced by the stratospheric conditions. These results are in line with a number of previous studies that using data for the middle and low latitudes of both hemispheres showed the ionospheric response to the SSW event in 2013. Nonetheless, to our knowledge, this is the first time that the coupling between the stratosphere and ionosphere is shown for the Iberian Peninsula region. This coupling is most prominent for the stratospheric temperature during east-QBO winter with the SSW event, and, probably, depends on the QBO-phase.

## Acknowledgments, Samples, and Data

Anna Morozova was supported by the postdoc from the Fundação para a Ciência e a Tecnologia (FCT) scholarship SFRH/BPD/74812/2010.

Juan José Blanco was supported through the project CTM2016-77325-C2-1-P funded by Ministerio de Economía y Competitividad.

CITEUC is funded by National Funds through FCT — Foundation for Science and Technology (project UID/Multi/00611/2013) and FEDER — European Regional Development Fund through COMPETE2020 — Operational Programme Competitiveness and Internationalization (project POCI-01-0145-FEDER-006922).

Sounding data were obtained through the GRA database <http://www.ncdc.noaa.gov/data-access/weather-balloon/integrated-global-radiosonde-archive> and University of Wyoming, College of Engineering, Department of Atmospheric Science <http://weather.uwyo.edu/upperair/sounding.html>.

Zonally averaged stratospheric temperature and zonal wind data were downloaded from the MERRA websites <http://gmao.gsfc.nasa.gov/research/merra/> and [http://acdb-ext.gsfc.nasa.gov/Data\\_services/met/ann\\_data.html](http://acdb-ext.gsfc.nasa.gov/Data_services/met/ann_data.html).

We acknowledge the use of the area-averaged data on the stratospheric temperature and ozone from AIRS Science Team/Joao Texeira, 2012, last updated 2013: AIRX3STD v006.NASA/GSFC, Greenbelt, MD, USA, NASA Goddard Earth Sciences Data and Information Services Center (GES DISC). Accessed at 10.5067/AQUA/AIRS/DATA301. The data were obtained through Giovanni online data system, developed and maintained by the NASA GES DISC <http://giovanni.sci.gsfc.nasa.gov/giovanni>.

The data on the QBO phases are from the Department of Earth Sciences of the Freie Universität Berlin <http://www.geo.fu-berlin.de/met/ag/strat/produkte/qbo>.

CaLMA cosmic ray flux data are available from NMDB website <http://www.nmdb.eu/nest/search.php>.

Geomagnetic data measured by the GAO UC are available by request ([pribeiro@ci.uc.pt](mailto:pribeiro@ci.uc.pt)); the hourly values for the X, Y, and Z components from 2007 to 2014 can be also found at <https://doi.pangaea.de/10.1594/PANGAEA.863008>.

We acknowledge the use of the Dst index from the Kyoto World Data Center <http://wdc.kugi.kyoto-u.ac.jp/dstae/index.html>.

The Mg II data are from Institute of Environmental Physics, University of Bremen <http://www.iup.uni-bremen.de/gome/gomemgii.html>.

We also wish to thank the Ebro Observatory and Dr. Germán Solé for the provision of ionosonde data.

We acknowledge the mission scientists and principal investigators who provided the data used in this research.

We acknowledge Dr. H. Ye and his colleagues who provide implementation of the CCM analysis as an R package available at <https://cran.r-project.org/package=rEDM>.

## References

- Altadill, D., and E.M. Apostolov (2001), Vertical propagating signatures of wave-type oscillations (2-and 6.5-days) in the ionosphere obtained from electron-density profiles. *J. Atmos. Sol.-Terr. Phys.*, 63(9), pp.823-834.
- Altadill, D., and E. M. Apostolov (2003), Time and scale size of planetary wave signatures in the ionospheric F region: Role of the geomagnetic activity and mesosphere/lower thermosphere winds, *J. Geophys. Res.*, 108(A11), 1403, doi:10.1029/2003JA010015.
- Butler, A.H., J.P. Sjöberg, D.J. Seidel and K.H. Rosenlof (2017), A sudden stratospheric warming compendium. *Earth Sys. Sci. Data*, 9(1), p.63
- Bramberger, M., A. Dörnbrack, K. Bossert, B. Ehard, D. C. Fritts, B. Kaifler, C. Mallaun, A. Orr, P. Pautet, M. Rapp, and M. J. Taylor (2017), Does Strong Tropospheric Forcing Cause Large-Amplitude Mesospheric Gravity Waves? A DEEPWAVE Case Study. *J. Geophys. Res.-Atmospheres*, 122(21).
- Cander, L. R. (2016), Re-visit of ionosphere storm morphology with TEC data in the current solar cycle. *J. Atmos. Sol.-Terr. Phys.*, 138, 187-205, doi:10.1016/j.jastp.2016.01.008.
- Cander, L. R. and Mihajlovic, S. J. (1998), Forecasting ionospheric structure during the great geomagnetic storms, *J. Geophys. Res.: Space Phys.*, 103 (A1), 391–398, doi:10.1029/97JA02418.
- Chapman, S.J., and J. Bartels (1951), *Geomagnetism*, Vol. 1, Clarendon Press, 542 pp.
- Chen, Y., L. Liu, H. Le, and W. Wan (2018) Responses of solar irradiance and the ionosphere to an intense activity region. *J. Geophys. Res.: Space Phys.*, 123(3), 2116-2126, doi:10.1002/2017JA024765.
- Chen, G., C. Wu, S. Zhang, B. Ning, X. Huang, D. Zhong, H. Qi, J. Wang, and L. Huang (2016), Midlatitude ionospheric responses to the 2013 SSW under high solar activity, *J. Geophys. Res.-Space*, 121, 790–803, doi:10.1002/2015JA021980.
- Chernigovskaya, M.A., B.G. Shpynev, and K.G. Ratovsky (2015) Meteorological effects of ionospheric disturbances from vertical radio sounding data. *J. Atmos. Sol.-Terr. Phys.*, 136, pp.235-243.
- Cleveland, R. B., W. S. Cleveland, J. E. McRae, and I. Terpenning (1990), STL: A seasonal-trend decomposition procedure based on LOESS, *J. Off. Stat.*, 6, 3–73.
- Cleveland, W. S. (1979), Robust locally weighted regression and smoothing scatterplots, *J. Am. Stat. Assoc.*, 74(368), 829–836.
- Cleveland, W. S., and S. J. Devlin (1988), Locally weighted regression: An approach to regression analysis by local fitting, *J. Am. Stat. Assoc.*, 83(403), 596–610, doi:10.2307/2289282.
- Coy, L. and S. Pawson (2015), The major stratospheric sudden warming of January 2013: analyses and forecasts in the GEOS-5 data assimilation system. *Mon. Weather Rev.*, 143(2), 491-510.
- Danilov, A. (2017), New results in studying foF2 trends. *J. Atmos. Sol.-Terr. Phys.*, 163, 103-113, doi:10.1016/j.jastp.2017.04.002.
- Ebisuzaki, W. (1997), A method to estimate the statistical significance of a correlation when the data are serially correlated, *J. Clim.*, 10(9), 2147–2153.

- Ern, M., Q. T. Trinh, M. Kaufmann, I. Krisch, P. Preusse, J. Ungermann, Y. Zhu, J. C. Gille, M. G. Mlynczak, J. M. Russell III, M. J. Schwartz, and M. Riese (2016), Satellite observations of middle atmosphere gravity wave absolute momentum flux and of its vertical gradient during recent stratospheric warmings, *Atmos. Chem. Phys.*, 16, 9983-10019, <https://doi.org/10.5194/acp-16-9983-2016>.
- Ern, M., Q. T. Trinh, P. Preusse, J. C. Gille, J. C., M. G. Mlynczak, J. M. Russell III, and M. Riese (2018), GRACILE: A comprehensive climatology of atmospheric gravity wave parameters based on satellite limb soundings, *Earth Syst. Sci. Data*, 10, 857-892, [doi.org/10.5194/essd-10-857-2018](https://doi.org/10.5194/essd-10-857-2018).
- Flury, T., Hocke, K., Haefele, A., Kämpfer, N. and Lehmann, R., 2009. Ozone depletion, water vapor increase, and PSC generation at midlatitudes by the 2008 major stratospheric warming. *J. Geophys. Res.: Atmospheres*, 114(D18), 10.1029/2009JD011940.
- Forbes, J.M., S.E. Palo, and X. Zhang (2000), Variability of the ionosphere. *J. Atmos. Sol.-Terr. Phys.*, 62(8), pp.685-693.
- Fritts, D. C., and M. J. Alexander (2003), Gravity wave dynamics and effects in the middle atmosphere, *Rev. Geophys.*, 41(1), 1003, [doi:10.1029/2001RG000106](https://doi.org/10.1029/2001RG000106).
- Gavrilov, N.M., A.V. Koval, A.I. Pogoreltsev, and E.N. Savenkova (2018), Simulating planetary wave propagation to the upper atmosphere during stratospheric warming events at different mountain wave scenarios. *Adv. Space Res.*, 61, 7, 1819-1836, [doi:10.1016/j.asr.2017.08.022](https://doi.org/10.1016/j.asr.2017.08.022).
- Goncharenko, L. P., A. J. Coster, R. A. Plumb, D. I. Domeisen (2012), The potential role of stratospheric ozone in the stratosphere-ionosphere coupling during stratospheric warmings. *Geophys. Res. Lett.*, 39(8), [doi: 10.1029/2012GL051261](https://doi.org/10.1029/2012GL051261).
- Goncharenko, L., J. L. Chau, P. Condor, A., Coster, and L. Benkevitch (2013), Ionospheric effects of sudden stratospheric warming during moderate-to-high solar activity: Case study of January 2013. *Geophys. Res. Lett.*, 40(19), 4982-4986.
- Goncharenko, L., and S.R. Zhang (2008), Ionospheric signatures of sudden stratospheric warming: Ion temperature at middle latitude. *Geophys. Res. Lett.*, 35(21).
- Grewe, V. (2006) The origin of ozone. *Atmos. Chem. Phys.*, 6(6), pp.1495-1511.
- Holton, J.R. and H.C. Tan (1982), The quasi-biennial oscillation in the Northern Hemisphere lower stratosphere. *Journal of the Meteorological Society of Japan. Ser. II*, 60(1), 140-148.
- Huang, K.M., Z.X. Yang, R. Wang, S.D. Zhang, C.M. Huang, F. Yi, and F. Hu (2018), A statistical study of inertia gravity waves in the lower stratosphere over the Arctic region based on radiosonde observations, *J. Geophys. Res.-Atmos.*, 123, 10, 4958-4976.
- Jin, H., Y. Miyoshi, D. Pancheva, P. Mukhtarov, H. Fujiwara, and H. Shinagawa (2012), Response of migrating tides to the stratospheric sudden warming in 2009 and their effects on the ionosphere studied by a whole atmosphere-ionosphere model GAIA with COSMIC and TIMED/SABER observations. *J. Geophys. Res.Space Phys.*, 117, A10323, [doi:10.1029/2012JA017650](https://doi.org/10.1029/2012JA017650).



- Jonah, O. F., E. R. Paula, E. A. Kherani, S. L. G. Dutra, and R. R. Paes (2014), Atmospheric and ionospheric response to sudden stratospheric warming of January 2013. *J. Geophys. Res.-Space*, 119(6), pp.4973-4980.
- Kazimirovsky, E., M., Herraiz, and B.A. De la Morena (2003) Effects on the ionosphere due to phenomena occurring below it. *Surv. Geophys.*, 24(2), 139-184, doi:10.1023/A:1023206426746.
- Kazimirovsky, E.S., and V.D. Kokourov (1991), *J. Geomag. Geoelectr.* 43 (Suppl), 551-562
- Keil, M., D. R. Jackson, and M. C. Hort (2007), The January 2006 low ozone event over the UK. *Atmos. Chem. Phys.*, 7(3), pp.961-972.
- Knížová, P.K., Z. Mošna, D. Kouba, K. Potužníková, and J. Boška (2015), Influence of meteorological systems on the ionosphere over Europe. *J. Atmos. Sol.-Terr. Phys.*, 136, pp.244-250.
- Kumar, V. V., and M. L. Parkinson (2017), A global scale picture of ionospheric peak electron density changes during geomagnetic storms, *Space Weather*, 15 (4), 637–652, doi:10.1002/2016SW001573.
- Künsch, H. R. (1989), The jackknife and the bootstrap for general stationary observations, *Ann. Stat.*, 17, 1217–1241.
- Lahiri, S. N. (1999), Theoretical comparisons of block bootstrap methods, *Ann. Stat.*, 27, 386–404. Laštovička, J. (2006) Forcing of the ionosphere by waves from below. *J. Atmos. Sol.-Terr. Phys.*, 68(3), pp.479-497.
- Laštovička, J., P. Krizan, P. Šauli, and D. Novotná (2003), Persistence of the planetary wave type oscillations in foF2 over Europe. *Ann. Geophys.*, 21, 7, 1543-1552.
- Laštovička, J., P. Šauli, and P. Krizan (2006), Persistence of planetary wave type oscillations in the mid-latitude ionosphere. *Ann. Geophys.-Italy*, 49(6).
- Laštovička, J., S.C. Solomon, and L. Qian, (2012) Trends in the neutral and ionized upper atmosphere, *Space Sci. Rev.*, 168, 113-145, doi:10.1007/s11214-011-9799-3
- Leake, J.E., C. R. DeVore, J. P. Thayer, A. G. Burns, G. Crowley, H. R. Gilbert, J. D. Huba, J. Krall, M. G. Linton, V. S. Lukin, W. Wang (2014) Ionized plasma and neutral gas coupling in the sun's chromosphere and Earth's ionosphere/thermosphere, *Space Sci Rev* 184, 1-4 107-172, doi:10.1007/s11214-014-0103-1
- Lee, H., and A. K. Smith (2003), Simulation of the combined effects of solar cycle, quasi-biennial oscillation, and volcanic forcing on stratospheric ozone changes in recent decades. *J. Geophys. Res.-: Atmospheres*, 108, D24049, doi:10.1029/2001JD001503.
- Liu, H.L., W. Wang, A. D. Richmond, and R. G. Roble (2010), Ionospheric variability due to planetary waves and tides for solar minimum conditions. *J. Geophys. Res.-Space*, 115(A6).
- Lu, H., M. P. Baldwin, L. J. Gray, and M. J. Jarvis (2008), Decadal-scale changes in the effect of the QBO on the northern stratospheric polar vortex, *J. Geophys. Res.: Atmos.* (1984–2012), 113(D10).
- Maraun D. and J. Kurths (2004), Cross wavelet analysis: significance testing and pitfalls. *Nonlin. Processes Geophys.*, 11, 505–514.

- Martyn, D. F. (1953), The morphology of the ionospheric variations associated with magnetic disturbances, I. Variations at moderately low latitudes, *Proc. R. Soc. London, Ser. A*, 218, 1–18.
- Maruyama, T., G. Ma, and M. Nakamura (2009), Observations of TEC Disturbances with GEONET-TEC Storm and SED. *Journal of the National Institute of Information and Communications Technology*, 56(1-4), 349-368.
- Matsushita, S. (1968) Sq and L current systems in the ionosphere. *Geophy. J. Int.*, 15(1-2), 109-125.
- Medina, J., J. J. Blanco, O. García, R. Gómez-Herrero, E. J. Catalán, I. García, M. A. Hidalgo, D. Meziat, M. Prieto, J. Rodríguez-Pacheco, and S. Sánchez (2013), Castilla-La Mancha neutron monitor, *Nucl. Instrum. Meth. in Phy. Res. A: Accelerators, Spectrometers, Detectors and Associated Equipment*, 727, 97-103.
- Mendillo, M., H. Rishbeth, R. G. Roble, and J. Wroten (2002), Modelling F2-layer seasonal trends and day-to-day variability driven by coupling with the lower atmosphere, *J. Atmos. Sol.-Terr. Phy.*, 64, 1911–1931.
- Mohanakumar, K. (2008), *Stratosphere troposphere interactions: An introduction*, Springer Science & Business Media.
- Mønster, D., R. Fusaroli, K. Tylén, A. Roepstorff, and J. F. Sherson (2017), Causal inference from noisy time-series data—Testing the Convergent Cross-Mapping algorithm in the presence of noise and external influence. *Future Gener. Comp. Sy.*, 73, pp.52-62.
- Morozova, A. L., J. J. Blanco, and P. Ribeiro (2017), Modes of temperature and pressure variability in mid-latitude troposphere and lower stratosphere in relation to cosmic ray variations, *Space Weather*, 15, doi:10.1002/2016SW001582.
- Pancheva, D.V., and N. J. Mitchell (2004), Planetary waves and variability of the semidiurnal tide in the mesosphere and lower thermosphere over Esrange (68 N, 21 E) during winter. *J. Geophy. Res.-Space*, 109(A8).
- Pancheva, D., N. Mitchell, H. Middleton, and H. Muller (2003), Variability of the semidiurnal tide due to fluctuations in solar activity and total ozone. *J. Atmos. Sol.-Terr. Phy.*, 65(1), 1-19.
- Pancheva, D., and P. Mukhtarov (2011), Stratospheric warmings: The atmosphere–ionosphere coupling paradigm. *J. Atmos. Sol.-Terr. Phy.*, 73(13), pp.1697-1702.
- Pedatella, N. M. (2016), Impact of the lower atmosphere on the ionosphere response to a geomagnetic superstorm, *Geophy. Res. Lett.*, 43, 9383–9389. <https://doi.org/10.1002/2016GL07059>
- Pedatella, N. M., and J. M. Forbes (2010), Evidence for stratosphere sudden warming–ionosphere coupling due to vertically propagating tides, *Geophy. Res. Lett.*, 37, L11104, doi:10.1029/2010GL043560.
- Pedatella, N. M., and H.-L. Liu (2018), The influence of internal atmospheric variability on the ionosphere response to a geomagnetic storm, *Geophy. Res. Lett.*, 45, 4578–4585, doi:10.1029/2018GL077867.
- Phanikumar, D. V., K. N. Kumar, and S. Kumar (2014), Signatures of ultra fast Kelvin waves in low latitude ionospheric TEC during January 2009 stratospheric warming event, *J. Atmos. Sol.-Terr. Phy.*, 117, 48-53.

- Randel, W. J., and J. B. Cobb (1994), Coherent variations of monthly mean total ozone and lower stratospheric temperature. *J. Geophys. Res.-Atmos.*, 99, D3, 5433–5447.
- Rishbeth, H., I. C. F. Müller-Wodarg, L. Zou, T. J. Fuller-Rowell, G. H. Millward, R. J. Moffett, D. W. Idenden, and A. D. Aylward (2000), Annual and semiannual variations in the ionospheric F2-layer: II. Physical discussion, *Ann. Geophys.*, 18( 8), 945-956.
- Roux, S.G., P.K. Knížová, Z. Mošna, and P. Abry, (2012), Ionosphere fluctuations and global indices: A scale dependent wavelet-based cross-correlation analysis. *J. Atmos. Sol.-Terr. Phys.*, 90, pp.186-197, doi:10.1016/j.jastp.2012.03.014.
- Sato, T. (1957), Disturbances in the ionospheric F2 region associated with geomagnetic storms II. Middle latitudes, *J. Geomagn. Geoelectr.*, 9, 1–22.
- Schiecke, K., B. Pester, M. Feucht, L. Leistritz, and H. Witte (2015), Convergent Cross Mapping: Basic concept, influence of estimation parameters and practical application, Engineering in Medicine and Biology Society (EMBC), 37th Annual International Conference of the IEEE, 7418-7421.
- Shpynev, B. G., V. I. Kurkin, K. G. Ratovsky, M. A. Chernigovskaya, A. Y. Belinskaya, S. A. Grigorieva, A. E. Stepanov, V. V. Bychkov, D. Pancheva, D., and P. Mukhtarov (2015), High-midlatitude ionosphere response to major stratospheric warming. *Earth Planets Space*, 67(18), doi:10.1186/s40623-015-0187-1
- Snively, J.B. (2017), Nonlinear Gravity Wave Forcing as a Source of Acoustic Waves in the Mesosphere, Thermosphere, and Ionosphere, *Geophys. Res. Lett.*, 44(23).
- Snow, M., M. Weber, J. Machol, R. Viereck, and E. Richard (2014), Comparison of Magnesium II core-to-wing ratio observations during solar minimum 23/24, *J. Space Weather Space Clim.*, 4, A04, doi:10.1051/swsc/2014001.
- Solomonov, S.V., E. P. Kropotkina, S. B. Rozanov, A. N. Ignat'ev, and A. N. Lukin (2017), Influence of strong sudden stratospheric warmings on ozone in the middle stratosphere according to millimeter wave observations. *Geomagn. Aeronomy*, 57(3), pp.361-368.
- Sridharan, S. (2017). Variabilities of lowlatitude migrating and nonmigrating tides in GPS-TEC and TIMED-SABER temperature during the sudden stratospheric warming event of 2013. *J. Geophys. Res.-Space Phys.*, 122, 10,748–10,761, doi:10.1002/2017JA024283
- Sugihara, G., R. May, H. Ye, C. H. Hsieh, E. Deyle, M. Fogarty, and S. Munch (2012), Detecting causality in complex ecosystems, *Science*, 338(6106), 496-500.
- Takens, F. (1981), Detecting strange attractors in turbulence, in: *Dynamical Systems and Turbulence, Lecture Notes in Mathematics*, Eds. D. A. Rand, and L.-S. Young, 898, Springer-Verlag, pp. 366–381.
- Torrence, C. and G.P. Compo (1998), A practical guide to wavelet analysis. *Bull. Amer. Meteor. Soc.* 79, 61-78.
- Tsonis, A.A., E.R. Deyle, H. Ye, and G. Sugihara (2018), Convergent Cross Mapping: Theory and an Example, *Adv. Nonlinear Geosc.*, 587-600.
- Tsonis, A.A., E.R. Deyle, R.M. May, G. Sugihara, K. Swanson, J.D Verbeten, and G. Wang (2015), Dynamical evidence for causality between galactic cosmic rays and

- interannual variation in global temperature. *P. Natl. Acad. Sci. USA*, 112(11), pp.3253-3256.
- van Nes, E.H., M. Scheffer, V. Brovkin, T. M. Lenton, H. Ye, E. Deyle, and G. Sugihara (2015), Causal feedbacks in climate change. *Nat. Clim. Change*, 5(5), pp.445-448.
- Yamazaki, Y., K. Häusler, and J.A. Wild (2016), Day-to-day variability of midlatitude ionospheric currents due to magnetospheric and lower atmospheric forcing. *J. Geophys. Res.: Space Phys.*, 121(7), 7067-7086.
- Yiğit, E., P.K. Knížová, K. Georgieva, and W. Ward (2016), A review of vertical coupling in the Atmosphere–Ionosphere system: Effects of waves, sudden stratospheric warmings, space weather and of solar activity. *J. Atmos. Sol.-Terr. Phys.*, 141, 1-12.
- Zhang, Y. and L.J. Paxton (2018), Solar EUV Flux Proxy Using Multifrequency Solar Radio Flux, *Space Weather*, 16, 5, 434-441, doi:10.1029/2017SW001763.

## **Appendix A. Glossary**

AC/noAC series	annual cycle series/series without annual cycle
CR	cosmic ray
cSVD	coupled singular value decomposition
gph	geopotential height
Mg II	composite series of the solar UV radiation
O <sub>3</sub>	ozone
PC	principal component
PCA	principal component analysis
QBO	quasi-biennial oscillation, eQBO/wQBO – west/east QBO phase
SSW	sudden stratospheric warming
T	temperature
TEC	total electron content
UV	ultra-violet



**Temperature and pressure variability in mid-latitude low atmosphere and stratosphere-ionosphere coupling**

**A. L. Morozova<sup>1</sup>, P. Ribeiro<sup>1,2</sup>, J. J. Blanco<sup>3</sup>, and T.V. Barlyaeva<sup>1</sup>**

<sup>1</sup>CITEUC, University of Coimbra, Almas de Freire, Sta. Clara, Coimbra, 3040-004, Portugal.

<sup>2</sup> Geophysical and Astronomical Observatory, University of Coimbra, Almas de Freire, Sta. Clara, Coimbra, 3040-004, Portugal.

<sup>3</sup> University of Alcalá, Pza. San Diego, s/n, 28801 Alcalá de Henares, Madrid, Spain.

**Contents of this file**

Figures S1 to S8.

**Introduction**

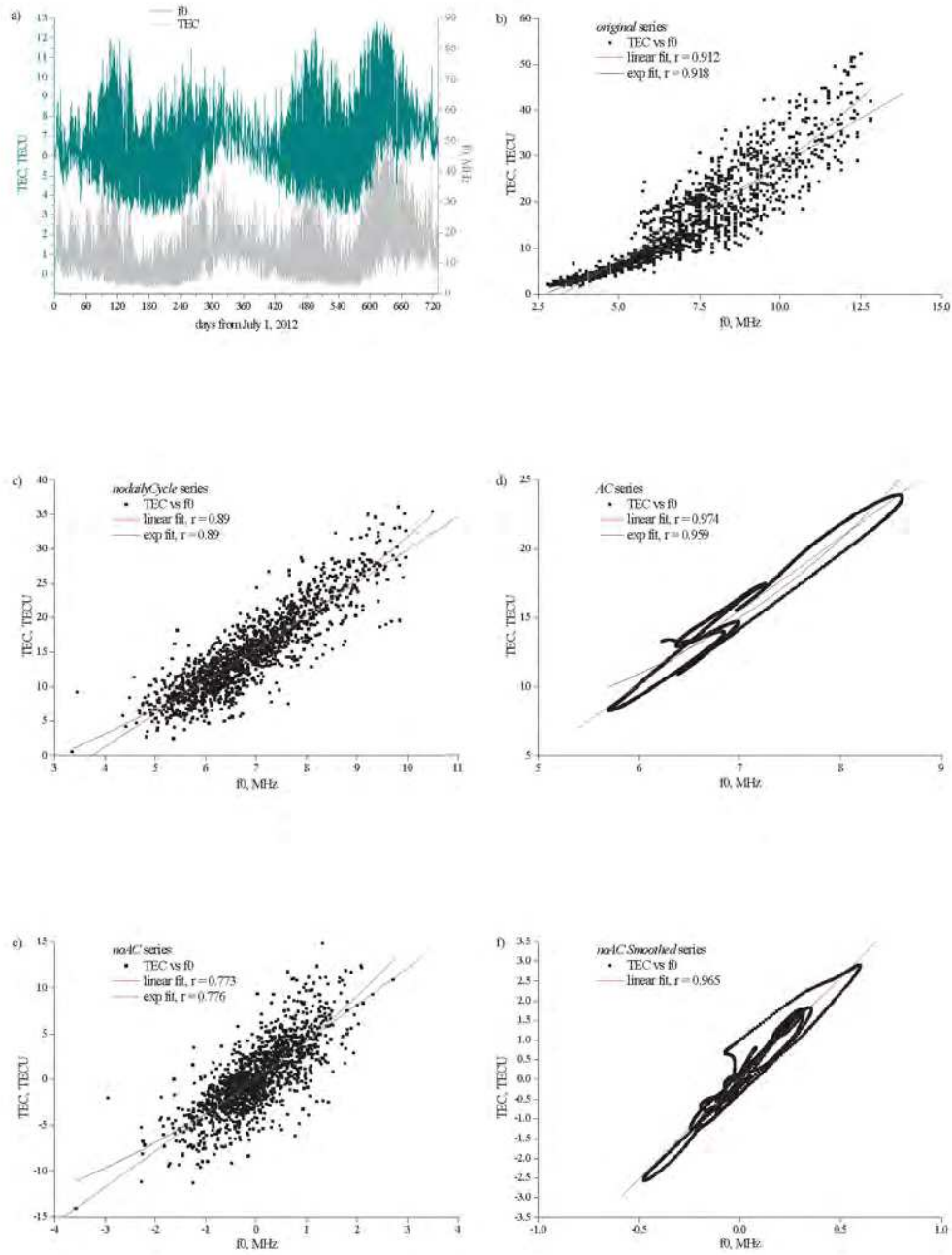
This file provides complementary information to topics discussed in the main article.

Figure S1 shows relations between the  $f_0F2$  and  $TEC$  parameters obtained at the Ebre Observatory. Since  $TEC$  calculations are based on  $f_0F2$  values, these two parameters are strongly correlated. Such correlations are observed on all time scales: bi-daily and daily data (Fig. S1b-c and S1e), annual variations (Fig. S1d) and variations with time scale from weeks to months (fig. S1f). Two fitting functions are shown: linear (red lines) and exponential (blue lines). The correlations coefficients (shown in legends) are high and have the same magnitude for both fitting functions.

Figures S2 and S5 show wavelet spectra for  $TEC$ ,  $O_{3\ 10}$ ,  $COI\ H$  and  $Mg\ II\ noAC$  series (Fig. S2) and for the PCA/cSVD PCs of the mode 2 for  $T$  and  $gph$  series (Fig. S5).

Figures S3, S4 and S7 show results of the CCM and wavelet cross-coherence analyses of  $TEC$  vs  $Mg\ II$  and of  $TEC$  vs  $COI\ H$  (Fig. S3), of  $O_{3\ 10}$  vs  $Mg\ II$  (Fig. S4) and of mode 2 PCA PCs vs  $O_{3\ 10}$  (Fig. S5).

Figures S6 and S8 present wavelet cross-coherence spectra for mode 2 cSVD PCs vs  $TEC$  (Fig. S6) and for mode 2 cSVD PCs vs  $O_{3\ 10}$  (Fig. S8).



**Figure S1.** (a) Time variations of f0F2 and TEC series obtained at the Ebre Observatories. (b-f) Scatter plots of TEC vs f0F2 for the original data (b), series with removed daily cycle (c), AC series (d), noAC series (e) and Smoothed series (f). Red lines are linear and blue lines are exponential fits. Corresponding correlation coefficients  $r$  are shown in legends.

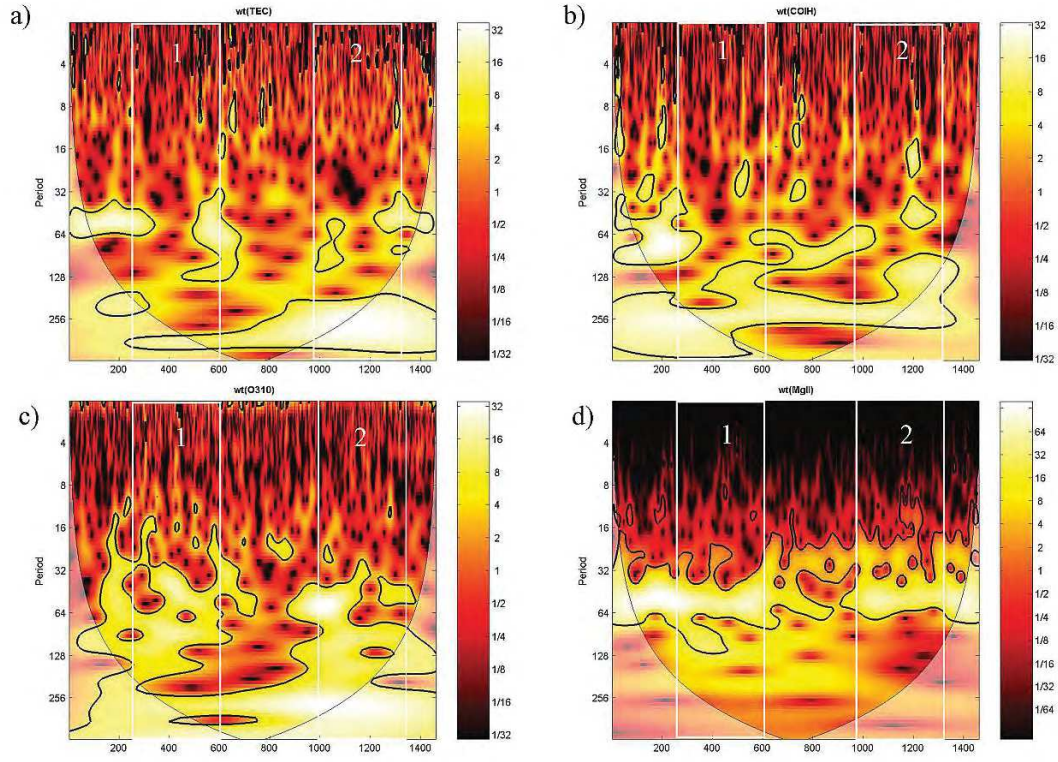


**Figure S2.** Wavelet spectra *TEC* (a), *COI H* (b), *O<sub>3 10</sub>* (c) and *Mg II* (d) *noAC* series or the whole time interval (1460 pts, counted in 0.5\*day starting from July 1, 2012). White rectangles mark *eQBO* (“1”) and *wQBO* (“2”) winters. Statistically significant values are inside the black contours. Area outside of cones of influence is shaded. The period is in half-days (e.g., period = 32 equals to the period of 16 days).

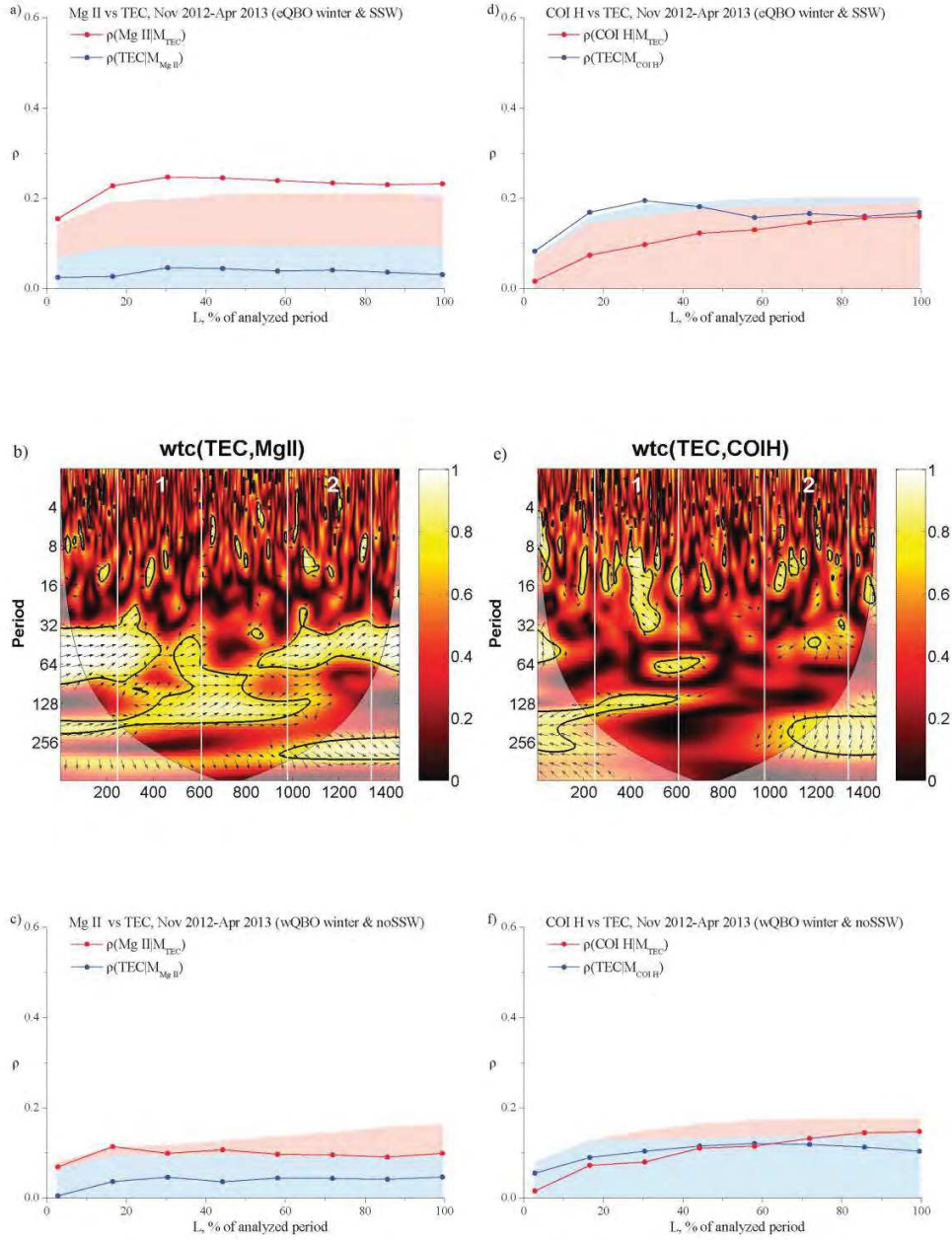


**Figure S3.** Left: Results of the CCM analysis the  $TEC$  vs  $Mg II$  for the  $eQBO$  (a) and  $wQBO$  (c) winters. The skill of cross-map estimates, indicated by the correlation coefficient ( $\rho$ ), varies with the library length  $L$  shown as a percentage of the analyzed time interval (362 points). Red lines are reconstructions of  $Mg II$  from  $TEC$ , blue lines are reconstructions of  $TEC$  from  $Mg II$ . Shaded areas show 95% significance level. Wavelet cross-coherence spectrum (b) for the whole time interval (1460 pts, counted in  $0.5 \cdot \text{day}$  starting from July 1, 2012) between  $Mg II$  and  $TEC$ . White rectangles mark  $eQBO$  ("1") and  $wQBO$  ("2") winters. Statistically significant values are inside the black contours. Area outside of cones of influence is shaded. The period is in  $0.5 \cdot \text{day}$  (e.g., period = 32 equals to the period of 16 days). Right: same as left but for  $TEC$  vs  $COI H$ .

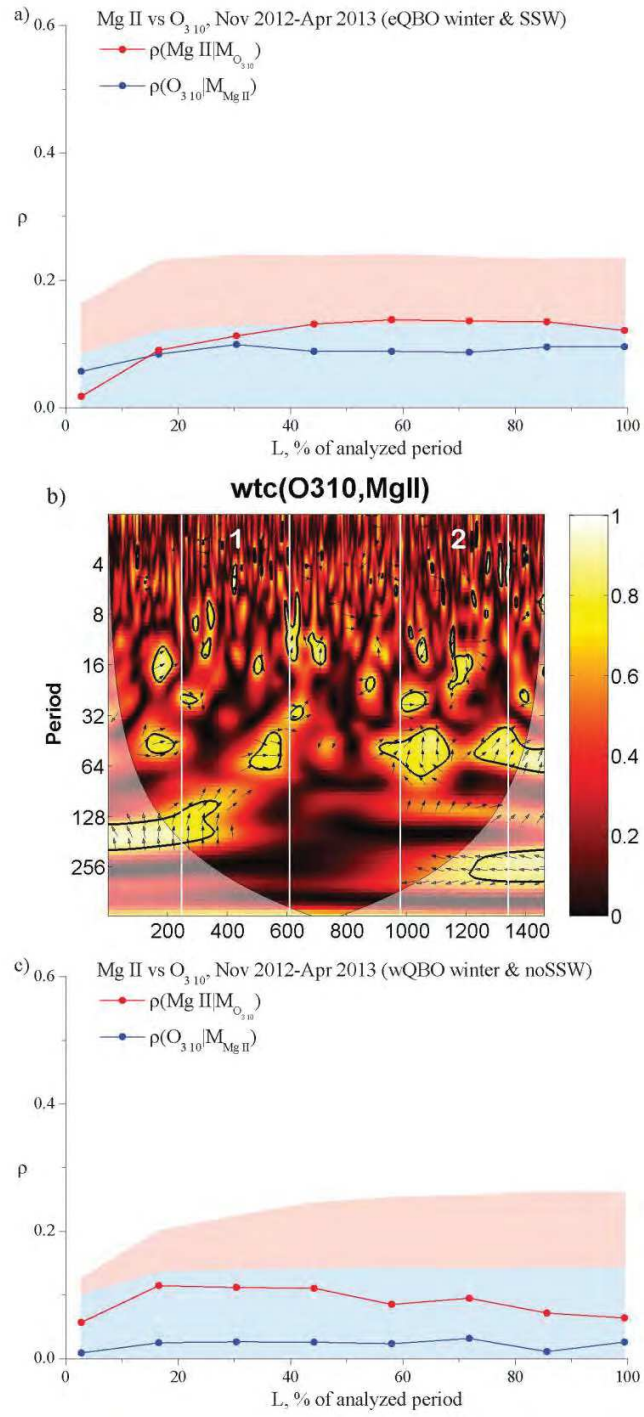


**Figure S4.** Same as Figure S3 but for  $O_{310}$  vs  $\text{Mg II}$ .



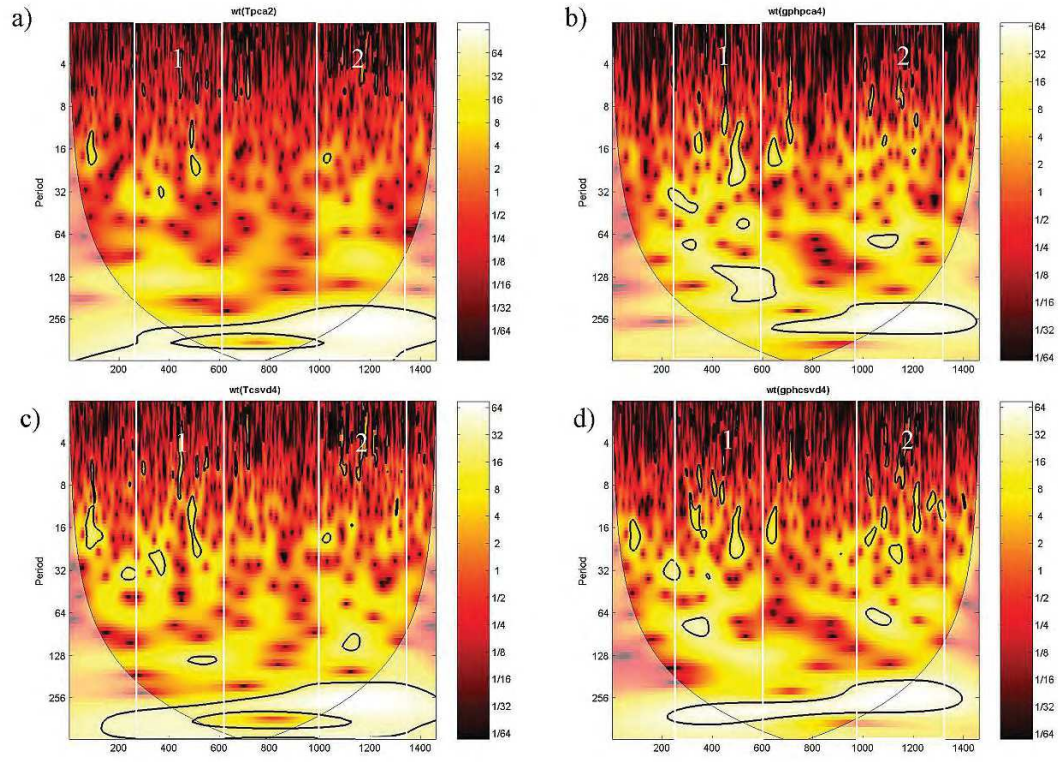


**Figure S5.** Same as in Figure S2 but for  $noAC$   $T_{PCA2}$  (a),  $gph_{PCA4}$  (b),  $T_{cSVD4}$  (c) and  $gph_{cSVD4}$  (d).

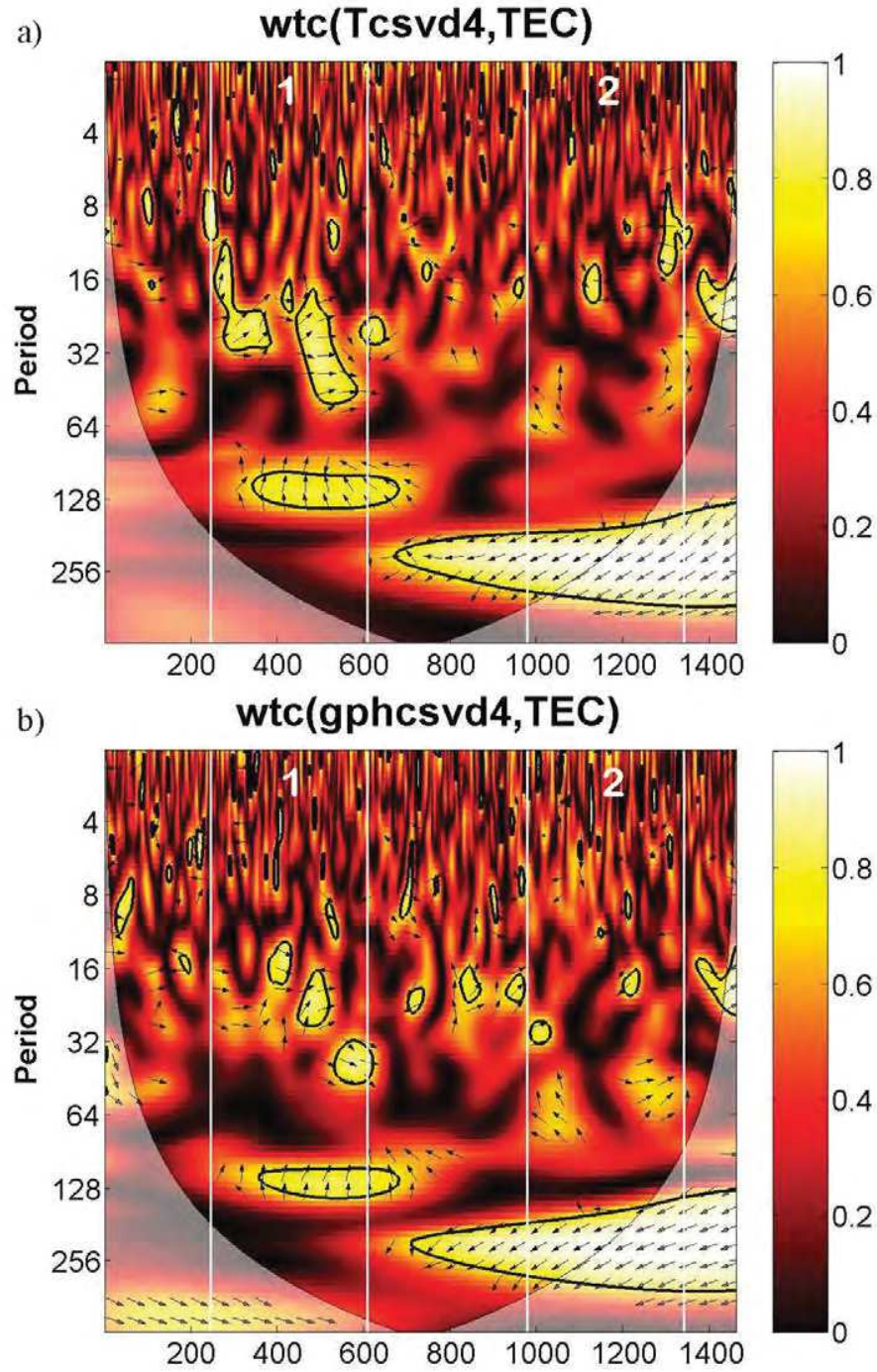


**Figure S6.** Wavelet cross-coherence spectrum for the whole time interval (1460 pts, counted in 0.5\*day starting from July 1, 2012)) between *TEC* and *T cSVD PC2* (**a**), and *gph cSVD PC2* (**b**).

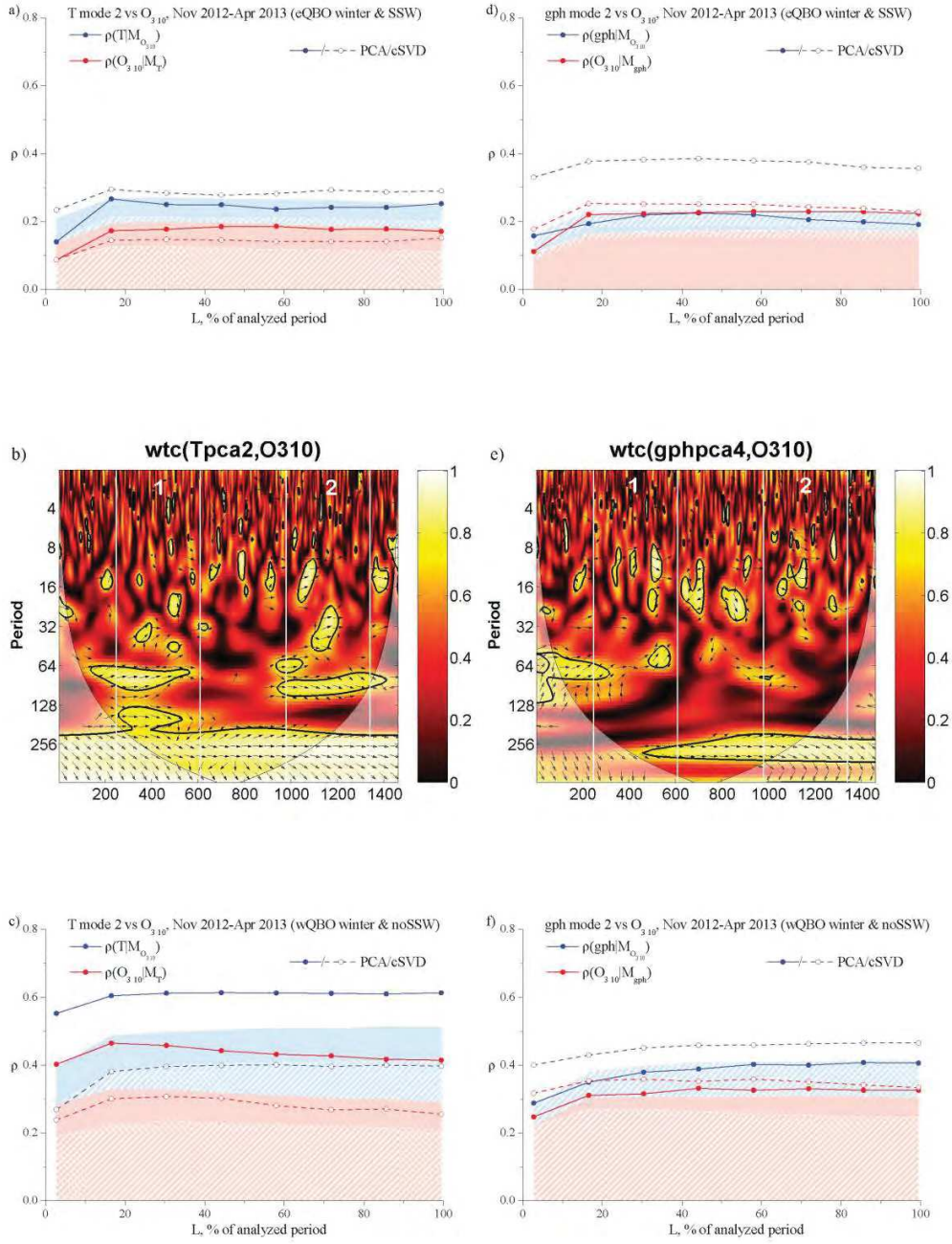


**Figure S7.** Same as Figure S3 but for  $O_{310}$  vs  $T$  PCs of the *noAC*  $T$  mode 2 (left) and for  $O_{310}$  vs *gph* PCs (right).



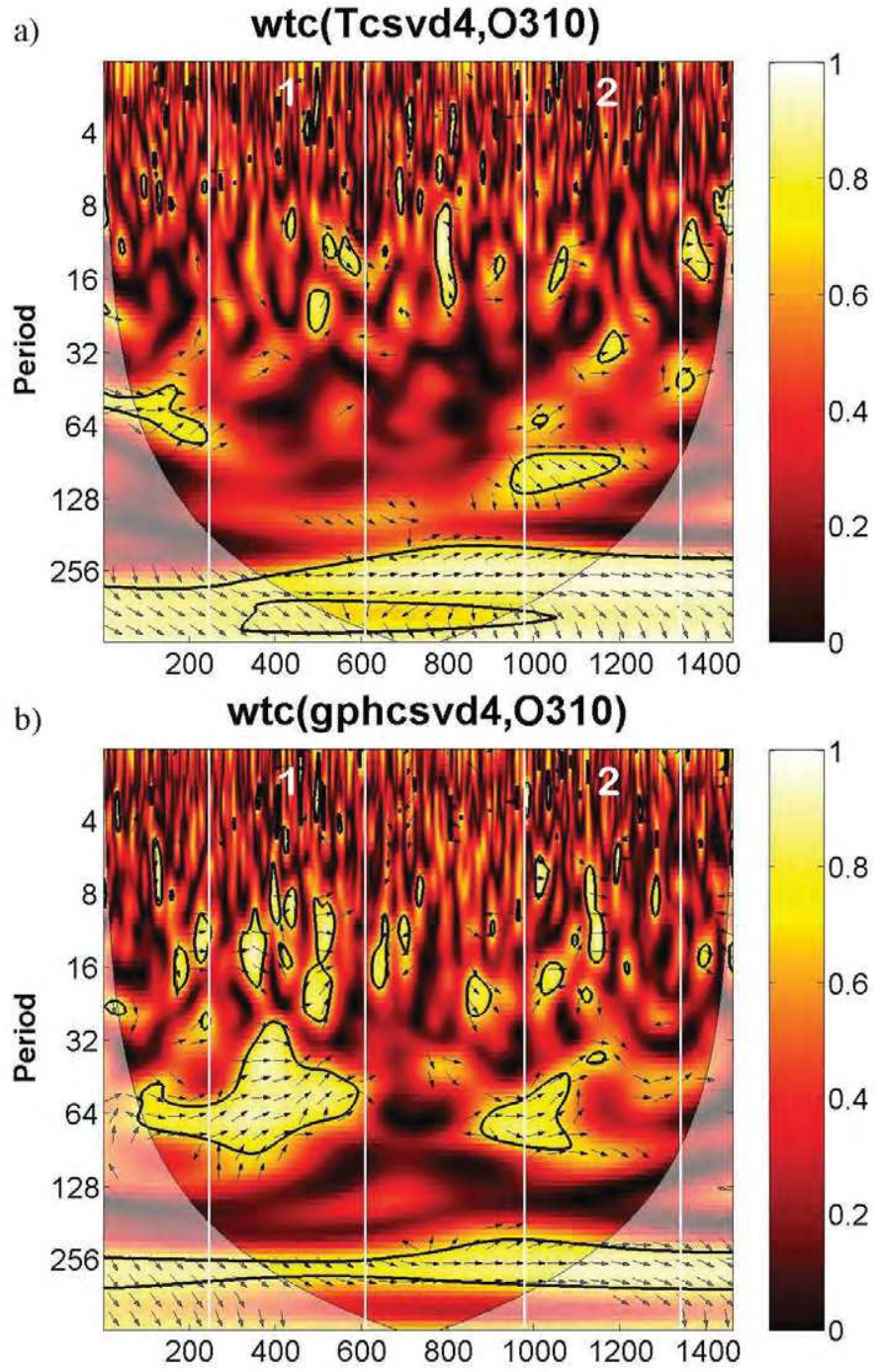


**Figure S8.** Same as Figure 6 but for  $O_{310}$  vs  $T$  cSVD PC2 (a), and vs  $gph$  cSVD PC2 (b).